Modelling megathrust earthquakes across scales: one-way coupling from geodynamics and seismic cycles to dynamic rupture

I. van Zelst[1], S. Wollherr[2], A.-A. Gabriel[2], E. H. Madden[2], Y. van Dinther[1,3]

[1]Seismology and Wave Physics, Institute of Geophysics, Department of Earth Sciences, ETH Zürich, Zürich, Switzerland
[2]Geophysics, Department of Earth and Environmental Sciences, LMU Munich, Munich, Germany
[3]Department of Earth Sciences, Utrecht University, Utrecht, The Netherlands

Key Points:

- We couple a geodynamic seismic cycle model to a dynamic rupture model to resolve subduction and earthquake dynamics across time scales
- Both events are comparable in terms of nucleation and material-dependent stress drop, but not slip
- Complex lithology leads to various rupture styles and speeds, shallow slip accumulation, and fault reactivation

Corresponding author: Iris van Zelst, `iris.vanzelst@erdw.ethz.ch`

Abstract

Taking the full complexity of subduction zones into account is important for realistic modelling and hazard assessment of subduction zone seismicity and associated tsunamis. Studying seismicity requires numerical methods that span a large range of spatial and temporal scales. We present the first coupled framework that resolves subduction dynamics over millions of years and earthquake dynamics down to fractions of a second. Using a two-dimensional geodynamic seismic cycle (SC) model, we model 4 million years of subduction followed by cycles of spontaneous megathrust events. At the initiation of one such SC event, we export the self-consistent fault and surface geometry, fault stress and strength, and heterogeneous material properties to a dynamic rupture (DR) model. Coupling leads to spontaneous dynamic rupture nucleation, propagation and arrest with the same spatial characteristics as in the SC model. It also results in a similar material-dependent stress drop, although dynamic slip is significantly larger. The DR event shows a high degree of complexity, featuring various rupture styles and speeds, precursory phases, and fault reactivation. Compared to a coupled model with homogeneous material properties, accounting for realistic lithological contrasts doubles the amount of maximum slip, introduces local pulse-like rupture episodes, and relocates the peak slip from near the downdip limit of the seismogenic zone to the updip limit. When an SC splay fault is included in the DR model, the rupture prefers the splay over the shallow megathrust, although wave reflections do activate the megathrust afterwards.

1 Introduction

Throughout the past decades, enigmatic observations of subduction zone earthquakes have repeatedly given rise to new insights. For example, large slip occurring up to the trench during the 2011 M_w9.0 Tōhoku-Oki earthquake demonstrated how poorly the occurrence of slip in shallow, presumably velocity-strengthening regions is understood to date (Fujiwara et al., 2011; Lay et al., 2011).

Understanding the seismic characteristics along megathrusts from the trench to the down-dip limit of the seismogenic zone is crucial for improving the assessment of seismic — and the associated tsunami — hazards. However, the physics governing subduction zone seismicity occurs on a wide range of temporal scales. Tectonic stresses build up over millions of years and are episodically released during earthquakes, which initiate, propagate, and stop on time scales smaller than seconds. Capturing the relevant physics across these time scales is computationally and numerically challenging and currently not yet feasible within a single modelling framework.

Geodynamic modelling usually tackles large scale, long-term problems, such as subduction zone evolution on a lithospheric or global scale over millions of years (see Billen, 2008; Gerya, 2011, for an overview). Such models provide insight into the formation and geometry of megathrust faults and the corresponding state of stress (Billen et al., 2003; Goes et al., 2017). However, most geodynamic models do not include elastic rheologies (Patočka et al., 2017) and resolve the physical processes on time scales on the order of thousands of years at most. These restrictions render them unsuitable for studying seismicity or earthquake rupture dynamics.

In contrast, seismic cycle models of the megathrust focus on smaller time scales spanning thousands of years down to coseismic time scales smaller than seconds (e.g., Rice, 1993; Ben-Zion & Rice, 1997; Lapusta et al., 2000; Liu & Rice, 2007; Langer et al., 2010; Kaneko et al., 2011). By modelling both long-term loading of predefined faults and spontaneous rupture across these faults, seismic cycle models can provide insight into interseismic stress build-up, coseismic rupture processes, and postseismic relaxation. However, the majority of seismic cycle models use quasi-static or quasidynamic approximations which do not account for the stresses mediated by the emitted seismic waves. Notable fully dynamic exceptions by, for example, Lapusta et al. (2000) and Kaneko et al. (2011), are algorithmically and computationally challenging.

Seismic cycle models are commonly limited to predefined faults, which are often simplified to planar geometries. These restrictions may result from the employed numerical scheme related to the spatial discretisation or the available computational resources. Furthermore, widely applied seismic cycle methods may inherently only account for homogeneous elastic media (Lapusta et al., 2000). While providing fundamental insight into the mechanics of the earthquake cycle, observations indicate multi-fault geometries and complex lithologies (e.g., Kodaira et al., 2002), which cannot yet be accounted for in state-of-the-art seismic cycle models.

Dynamic rupture models are designed to study the dynamics of earthquakes at coseismic time scales. Dynamic rupture modelling has been pioneered by e.g., Andrews (1973); Das (1980); Day (1982); Madariaga et al. (1998); Oglesby et al. (1998); Ampuero et al. (2002); Dalguer and Day (2007). Such models provide physically self-consistent earthquake source descriptions by modelling spontaneous frictional failure across a predefined fault coupled to seismic wave propagation. By using modern numerical methods and hardware specific software optimisation, dynamic rupture simulations can reach high spatial and temporal resolution of increasingly complex geometrical and physical modelling components (Wollherr, Gabriel, & Mai, 2019; Ulrich, Gabriel, et al., 2019). In comparison to the aforementioned approaches, such models fully incorporate inertia effects as well as the non-linear interaction of seismic waves and fault mechanics governed by friction.

However, the dynamic rupture community faces challenges in constraining the initial conditions governing fault stresses and strengths. These are integral ingredients of the dynamic rupture, as they govern the rupture propagation style (e.g., crack- versus pulse-like dynamics and sub- versus supershear rupture speeds), transfers (e.g., dynamic triggering potential), and earthquake arrest (e.g., Kame et al., 2003; Bai & Ampuero, 2017).

Another important open question is how to constrain the rupture nucleation process and hypocenter in a physically consistent manner. Dynamic rupture models typically use artificially enforced slip initiation by, e.g., locally reducing the static friction coefficient (Harris, 2004; Harris et al., 2009, 2011, 2018). However, the ensuing rupture is highly sensitive to the chosen nucleation approach and its computational resolution in time and space (Bizzarri, 2010; Gabriel et al., 2012, 2013; Galis et al., 2014). In addition, the location of the hypocenter may be chosen ad-hoc without a strong physical basis. Studying earthquake nucleation beyond ad-hoc approaches will further our understanding of the interaction of megathrust earthquakes, foreshocks and aseismic processes.

Ideally, the initial states of stress and fault strength are self-consistent and consistent with the geometry and rheology of the subsurface and fault networks. However, due to a lack of constraints, especially on the stress field, stresses, or fault normal and shear tractions are commonly prescribed as constant or linearly increasing with depth in dynamic rupture models (Kozdon et al., 2013; Kozdon & Dunham, 2013; Galvez et al., 2014, 2018). Direct measurements of on-fault stresses are difficult to obtain, but inferences from nearby borehole measurements and observations of stress orientations and rotations do provide insight on the shear and normal tractions acting on megathrusts (Chang et al., 2010; Hardebeck, 2012; Fulton et al., 2013; Hardebeck, 2015). Dynamic rupture models have incorporated such observations and also projected the inferred regional stress information onto spatially complex fault geometries (Aochi & Fukuyama, 2002; Aagaard et al., 2004; Gabriel & Pelties, 2014; Heinecke et al., 2014; Uphoff et al., 2017; Bauer et al., 2017; Ulrich, Gabriel, et al., 2019; Ulrich, Vater, et al., 2019; Wollherr et al., 2018). However, it is difficult to account for variable loading on different fault segments, local lithological heterogeneities, stress and fault roughness, stress interactions between faults and their surroundings, and the different stages of faults within their seismic cycle (Herrendörfer, 2018; Romanet et al., 2018).

The in situ fault strength is equally hard to constrain. Most studies focus on experimentally constraining the frictional behaviour of rocks at coseismic slip velocities (Dieterich, 1979; Ruina, 1983; Di Toro et al., 2011; den Hartog et al., 2012). Drilling experiments and heat flow measurements provide to-scale insight on the frictional strength of megathrusts (Fulton et al., 2013). Observational studies indirectly infer the distribution of the pore fluid pressure ratio in subduction zones (Seno, 2009). Various modelling efforts are also aimed at understanding the role of fluids on the strength of the megathrust (Angiboust et al., 2012; Petrini et al., 2017). Despite these advances, a major challenge is the large scaling difference between natural subduction zones, small-scale laboratory experiments, and localised, isolated field measurements.

Due to their locations, the exact fault geometry of subduction zones is often unknown. Splay faults are seaward verging crustal faults that splay away from the main subduction megathrust interface at shallow depth. They may rupture in addition to or instead of parts of the megathrust. It has been suggested that these splay faults play an important role during tsunamigenesis, because they could potentially accommodate large vertical displacements (Fukao, 1979). Therefore, several dynamic rupture studies have investigated fault branching and splay fault activation, mostly using simplified geometries (Wendt et al., 2009; Tamura & Ide, 2011; DeDontney & Rice, 2012; Li et al., 2014; E. H. Madden et al., 2017; Uphoff et al., 2017). Choosing appropriate stress and strength for both the megathrust and the splay fault has been shown to crucially affect branching and dynamic triggering (DeDontney et al., 2012; DeDontney & Hubbard, 2012).

"Seismo-thermo-mechanical" models provide insight into complex subduction zone features, such as the role of rheology, temperature, and fault geometry and evolution, including spontaneously evolving splay faults (e.g., van Dinther et al., 2014; Herrendörfer et al., 2015; Corbi et al., 2017; Dal Zilio et al., 2018, 2019; Preuss et al., 2019). These models bridge the time scales of traditional geodynamic and seismic cycle models, as initiated by van Dinther, Gerya, Dalguer, Corbi, et al. (2013); van Dinther, Gerya, Dalguer, Mai, et al. (2013). The therein developed two-dimensional model includes the long-term dynamics of subduction, as well as short-term frictional slip transients. However, these models cannot resolve the inertial dynamics of slip events due to numerical restrictions. The minimum resolution is 5 years in time and 500 m in space. The limitations in spatio-temporal resolution were recently overcome for a strike-slip setup with the seismo-thermo-mechanical rate-and-state friction methodology (Herrendörfer et al., 2018). However, applying this methodology to the more challenging setting of a subduction zone does not yet result in accurately crossing all time scales. In a thermo-mechanically evolving subduction zone, tectonic loading is limited to hundreds of thousands of years, instead of millions of years. Besides that, slow slip events have a maximum slip rate on the order of 10^{-7} m/s (Herrendörfer, 2018). Sobolev and Muldashev (2017) model time scales down to minutes to resolve postseismic processes in addition to subduction evolution. Nevertheless, the challenge of fully resolving the subduction evolution in combination with rupture dynamics on coseismic time scales remains.

To overcome the limitations of each of these approaches, the hereafter presented coupling approach fully resolves the tectonic, seismic cycle (excluding the postseismic phase), and dynamic rupture time scales for the first time by linking a transient slip event of a geodynamic seismic cycle (SC) model to a dynamic rupture (DR) model. By adapting the full outcome of the SC model into initial conditions for the DR model in a physically consistent manner, we provide geometries of the fault and its surroundings, material properties, and fault stresses and strength. This enables us to study the complex mechanics of subduction zones and megathrust earthquakes in a physically consistent manner.

The work presented here is structured as follows. First, we summarise the SC and DR modelling approaches and their respective assumptions in Secs. 2 and 3. We then describe how we couple the material properties, stresses, geometry and strength conditions of a representative SC event to the DR model in Sec. 4, specifically in light of the different set of equations and assumptions both approaches use. We discuss the resulting state of stress from the long-term subduction evolution in Sec. 5.1 and compare the geodynamic (Sec. 5.2) and dynamic rupture (Sec. 5.3) events in Sec. 5.4. To assess the effect of the heterogeneous, temperature-dependent material properties from the SC model on the dynamic rupture, we conduct a series of models with increasing material complexity in Sec. 5.5. In addition to a single megathrust rupture, we investigate the coseismic rupture dynamics along an additional splay fault based on the fault structures visible in the SC model (Sec. 5.6). To ensure that the coupling method is robust, we test the effect of the two main assumptions we made in Sec. 6.1: an idealised Poisson's ratio governing seismic wave propagation in the DR model (Sec. 6.1.1) and a linear slip weakening approximation in the DR model of the rate-weakening friction used in the SC model (Sec. 6.1.2). In Sec. 6.2, we discuss several possible future lines of work that could address the current limitations of our approach. We summarise our most important findings in Sec. 7.

2 Geodynamic seismic cycle model

We use the seismo-thermo-mechanical (STM) version of the two-dimensional, visco-elasto-plastic, continuum I2ELVIS code to solve the long-term dynamics of subduction zone evolution and the subsequent seismic cycle (Gerya & Yuen, 2007; van Dinther, Gerya, Dalguer, Corbi, et al., 2013; van Dinther, Gerya, Dalguer, Mai, et al., 2013; van Dinther et al., 2014). First, we briefly describe the governing equations, rheology, failure criterion, and friction formulation. We then describe the model setup in Sec. 2.4. A full description of the methods can be found in Gerya and Yuen (2007) and van Dinther, Gerya, Dalguer, Mai, et al. (2013).

2.1 Governing equations

We solve the following set of conservation equations in a two-dimensional Cartesian coordinate system, derived from the principles of conservation of mass (1), momentum (2), and energy (3):

$$\nabla \cdot \mathbf{v} = 0, \tag{1}$$

$$\rho \frac{D\mathbf{v}}{Dt} = \nabla \cdot \boldsymbol{\sigma'} - \nabla P + \rho \mathbf{g}, \tag{2}$$

$$\rho C_p \left(\frac{DT}{Dt} \right) = -\nabla \mathbf{q} + H_a + H_s + H_r. \tag{3}$$

All symbols and terms used in these and the following equations are described in Table 1. The continuity equation (1) assumes an incompressible medium, i.e., Poisson's ratio $\nu = 0.5$. This is valid when pressure and temperature changes are small and therefore only minimally impact the volume of the material. The energy equation (3) describes conductive ($\nabla \mathbf{q}$) and advective heat transport (within the material derivative

Table 1. Nomenclature

Symbol	Parameter	Unit
Δx	Grid size	m
$\dot{\boldsymbol{\varepsilon}}_{e,v,p}$	(Elastic, viscous, plastic) Strain rate	s^{-1}
$\dot{\varepsilon}_{vp,II}$	Second invariant of the visco-plastic strain rate	s^{-1}
η, η_0	Viscosity, reference viscosity equal to $1/A_D$	Pa s
η_{vp}	Effective visco-plastic viscosity	Pa s
λ	Pore fluid pressure ratio P_f/P	-
λ_1	First Lamé parameter	Pa
$\mu^{\mathrm{sc,dr}}_{(\mathrm{eff})}$	(Effective) Friction coefficient (sc,dr)	-
$\mu^{\mathrm{sc,dr}}_{d}$	Dynamic friction coefficient (sc,dr)	-
$\mu^{\mathrm{sc,dr}}_{s}$	Static friction coefficient (sc,dr)	-
ν	Poisson's ratio	-
ρ, ρ_0	Density, reference density	kg m^{-3}
σ'_{II}	Second invariant of the deviatoric stress tensor	Pa
$\boldsymbol{\sigma}$, $\boldsymbol{\sigma'}$	Stress tensor, deviatoric stress tensor	Pa
σ_n	Normal stress	Pa
$\sigma^{\mathrm{sc,dr}}_{\mathrm{yield}}$	Yield stress (sc,dr)	Pa
$\sigma^{\mathrm{dr}}_{\mathrm{sliding}}$	DR sliding stress	Pa
τ	Shear stress	Pa
χ	Plastic multiplier	s^{-1}
A_D	Pre-exponential factor	Pa^{-n} s^{-1}
c	On-fault cohesion	Pa
C	Bulk cohesion	Pa
C_p	Isobaric heat capacity	J kg^{-1} K^{-1}
d	Slip	m
D_c	Characteristic slip distance	m
E_a	Activation energy	J mol^{-1}
f_{max}	Maximum resolved frequency	s^{-1}
F	Visco-elasticity factor	-
g	Gravity acceleration	m s^{-2}
G	Shear modulus	Pa
$G_{plastic}$	Plastic flow potential	Pa
H_a, H_r, H_s	Adiabatic, radioactive and shear heat production	W m^{-3}
n	Stress exponent	-
P, P_{eff}, P_f	(Solid rock, effective, pore fluid) Pressure	Pa
$\boldsymbol{q}$	Heat flux	W m^{-2}
R	Gas constant	J mol^{-1} K^{-1}
S	S parameter	-
t	Time	s
T	Temperature	K
$\mathbf{v}$	Velocity	m s^{-1}
v_p, v_s	P-, S-wave velocity	m s^{-1}
V	Slip rate	m s^{-1}
V_a	Activation volume	J Pa^{-1} mol^{-1}
V_c	Characteristic velocity	m s^{-1}
Z	Seismic impedance	kg s^{-1} m^{-2}

$\rho C_p\left(\frac{DT}{Dt}\right)$), and the internal heat generation due to adiabatic (de)compression H_a, shear heating during anelastic deformation H_s, and radioactive heat production H_r.

We use an implicit finite difference scheme on a fully staggered Eulerian grid to solve for the velocity $\mathbf{v}$, the solid rock pressure P, and the temperature T (Gerya & Yuen, 2007). We use second order spatial discretisation and first order temporal discretisation. Large deformation is numerically modelled by Lagrangian markers that are advected according to their velocity, while keeping track of the rock composition, associated material properties, and stress history (see Gerya & Yuen, 2003, and references therein). For a complete description of all the components of the heat equation used in this model, we refer to van Dinther, Gerya, Dalguer, Mai, et al. (2013).

2.2 Rheology

To solve the governing equations, we need constitutive equations that relate the stress and strain rate. We use a visco-elastic Maxwell rheology in combination with a frictional plastic slider (Gerya, 2010). The total strain rate is the sum of its elastic, viscous and plastic components:

$$\dot{\boldsymbol{\varepsilon}} = \frac{1}{2}\Big(\nabla\mathbf{v} + \nabla\mathbf{v}^T\Big) = \dot{\boldsymbol{\varepsilon}}_v + \dot{\boldsymbol{\varepsilon}}_e + \dot{\boldsymbol{\varepsilon}}_p. \tag{4}$$

The viscous strain rate component is

$$\dot{\boldsymbol{\varepsilon}}'_v = \frac{1}{2\eta}\boldsymbol{\sigma}', \tag{5}$$

where η is the effective viscosity and $\boldsymbol{\sigma}'$ is the deviatoric stress tensor.

The elastic strain rate component is described as

$$\dot{\boldsymbol{\varepsilon}}'_e = \frac{1}{2G}\frac{D\boldsymbol{\sigma}'}{Dt}. \tag{6}$$

It depends on the shear modulus G and the co-rotational stress rate $\frac{D\boldsymbol{\sigma}'}{Dt} = \frac{\boldsymbol{\sigma}'_{t+1}-\boldsymbol{\sigma}'_t}{\Delta t} + \dot{\boldsymbol{\omega}}\boldsymbol{\sigma} - \boldsymbol{\sigma}\dot{\boldsymbol{\omega}}$, where $\boldsymbol{\omega} = \frac{1}{2}\Big(\nabla\mathbf{v} - \nabla\mathbf{v}^T\Big)$ is the rotation tensor. The SC approach uses an explicit first-order finite difference scheme to solve for the elastic history. We also rotate the elastic stresses to account for local stress orientation changes due to the rotation of material points. More details on the treatment and implementation of elasticity can be found in Moresi et al. (2003); Gerya (2010); van Dinther, Gerya, Dalguer, Corbi, et al. (2013); Herrendörfer et al. (2018). The SC numerical method thus treats elasticity differently from the elastodynamic framework of the DR approach (Sec. 3). Additionally, the elastic strain rate in the incompressible SC model (Eq. 6) differs from the compressible formulation in the DR model (Eq. 14).

The plastic strain rate component is described as

$$\dot{\boldsymbol{\varepsilon}}'_p = \begin{cases} 0 & \text{if} \quad \sigma'_{\mathrm{II}} < \sigma^{\mathrm{sc}}_{\mathrm{yield}} \\ \chi\frac{\partial G_{\mathrm{plastic}}}{\partial \sigma'_{II}} & \text{if} \quad \sigma'_{\mathrm{II}} = \sigma^{\mathrm{sc}}_{\mathrm{yield}}. \end{cases} \tag{7}$$

In this plastic flow rule, G_{plastic} is the plastic potential of yielding material and χ is the plastic multiplier, which connects the components of the plastic strain rate with the local stress distribution σ'_{II}.

Table 2. Material parameters seismic cycle model

Material	Rock	Flow law[a]	η_0 $\left[\mathrm{Pa}^n\ \mathrm{s}\right]$	n [-]	E_a $\left[\mathrm{J\ mol}^{-1}\right]$	V_a $\left[\mathrm{J\ Pa}^{-1}\right]$	ρ_0^b $\left[\mathrm{kg\ m}^{-3}\right]$	G^c [GPa]	μ_s [-]	μ_d^i [-]	C [MPa]
Sticky air	-	-	$1.0 \cdot 10^{17}$	1	0	0	1	700	0	0	0
Incoming sediments	Sediments	Wet quartzite	$1.97 \cdot 10^{17}$	2.3	$1.54 \cdot 10^5$	$0.8 \cdot 10^{-5}$	2600	9.7262	0.35^d	0.105	2.5
Sediments	Sediments	Wet quartzite	$1.97 \cdot 10^{17}$	2.3	$1.54 \cdot 10^5$	$0.8 \cdot 10^{-5}$	2600	17	0.35^d	0.105	2.5
Upper oceanic crust	Basalt	Wet quartzite	$1.97 \cdot 10^{17}$	2.3	$1.54 \cdot 10^5$	$0.8 \cdot 10^{-5}$	3000	38	0.50^e	0.150	5^j
Lower oceanic crust	Gabbro	Plagioclase	$4.80 \cdot 10^{22}$	3.2	$2.38 \cdot 10^5$	$0.8 \cdot 10^{-5}$	3000	38	0.85^f	0.255	15
Upper continental crust	Sandstone	Wet quartzite	$1.97 \cdot 10^{17}$	2.3	$1.54 \cdot 10^5$	$1.2 \cdot 10^{-5}$	2700	34	0.72^g	0.216	10
Lower continental crust	Sandstone	Wet quartzite	$1.97 \cdot 10^{17}$	2.3	$1.54 \cdot 10^5$	$1.2 \cdot 10^{-5}$	2700	34	0.72^g	0.216	10
Lithospheric mantle	Peridotite	Dry olivine	$3.98 \cdot 10^{16}$	3.5	$5.32 \cdot 10^5$	$0.8 \cdot 10^{-5}$	3300	63	0.60^h	0.180	20
Asthenospheric mantle	Peridotite	Dry olivine	$3.98 \cdot 10^{16}$	3.5	$5.32 \cdot 10^5$	$0.8 \cdot 10^{-5}$	3300	72	0.60^h	0.180	20
Mantle weak zone	Peridotite	Wet olivine	$5.01 \cdot 10^{20}$	4.0	$4.70 \cdot 10^5$	$0.8 \cdot 10^{-5}$	3300	63	0.10	0.03	20

See van Dinther, Gerya, Dalguer, Mai, et al. (2013) for parameters related to the energy equation (3). Values obtained from: [a]Ranalli (1995) unless otherwise stated; [b]Turcotte and Schubert (2002); [c]Bormann et al. (2012); [d]Den Hartog et al. (2012); [e]Di Toro et al. (2011); [f]Tsutsumi and Shimamoto (1997); [g]e.g., Dieterich (1978); Chester and Higgs (1992); Di Toro et al. (2011); [h]Del Gaudio et al. (2009); [i] friction coefficient decreases to 30% of its initial value μ_s according to Di Toro et al. (2011); [j]Schultz (1995).

We consider dislocation creep with a non-linear viscosity η that depends on the second invariant of the stress tensor σ'_{II} (e.g., Ranalli, 1995):

$$\eta = \left(\frac{1}{\sigma'_{II}}\right)^{n-1} \cdot \frac{1}{2A_D} \cdot \exp\left(\frac{E_a + PV_a}{RT}\right), \tag{8}$$

where R is the gas constant and n, A_D, E_a, and V_a are material dependent viscous parameters (Table 1). Values for the material parameters for each rock type are constrained by experimental studies and can be found in Table 2.

2.3 Failure criterion and friction formulation

Brittle behaviour is characterised by Drucker-Prager plasticity (Drucker & Prager, 1952), which is commonly used in geodynamics (e.g., Kaus, 2010; Buiter et al., 2016). In this yield criterion, the second invariant of the deviatoric stress tensor $\sigma'_{II} = \sqrt{\sigma'^2_{xx} + \sigma'^2_{xz}}$ at a point in the rock is compared to the yield stress (or strength) $\sigma^{sc}_{\text{yield}}$ of the rock. Plastic failure in the form of spontaneous brittle instabilities occurs when the stress reaches the rock's yield stress. The yield stress of a rock depends on its cohesion C, its friction coefficient μ^{sc}, and the effective pressure P_{eff}, according to

$$\sigma^{sc}_{\text{yield}} = C + \mu^{\text{sc}} P_{\text{eff}}, \tag{9}$$

with P_{eff} defined as

$$P_{\text{eff}} = P - P_f = \Big(1 - \lambda\Big)P, \tag{10}$$

where P_f is the pore fluid pressure, such that λ is the pore fluid pressure ratio P_f/P. The solid rock pressure P is defined as the negative mean stress $-\frac{\sigma_{xx}+\sigma_{zz}}{2}$. We solve a simplified formulation of fluid flow processes including metamorphic (de)hydration reactions and compaction (e.g., Gerya & Meilick, 2011). These processes are driven by pressure, depth, and temperature.

We use a strongly slip rate-dependent friction formulation (van Dinther, Gerya, Dalguer, Corbi, et al., 2013) in which the friction coefficient μ^{sc} drops non-linearly from the static friction coefficient μ^{sc}_s to the dynamic friction coefficient μ^{sc}_d with increasing slip rate V, according to

$$\mu^{\text{sc}} = \frac{V_c \mu^{\text{sc}}_s + V \mu^{\text{sc}}_d}{V_c + V}, \tag{11}$$

where V_c is the characteristic velocity at which half of the friction drop occurs. The visco-plastic slip rate V is derived from the visco-plastic strain rate according to

$$V = 2\dot{\varepsilon}'_{vp,II} \Delta x, \tag{12}$$

where Δx is the minimum grid size.

2.4 Geodynamic seismic cycle model setup

We use a two-dimensional setup of a trench-normal section of the Southern Chilean subduction zone where the oceanic Nazca plate subducts beneath the continental South American plate. This setup is based on van Dinther, Gerya, Dalguer, Mai, et al. (2013) who validated this setup against GPS data before and during the

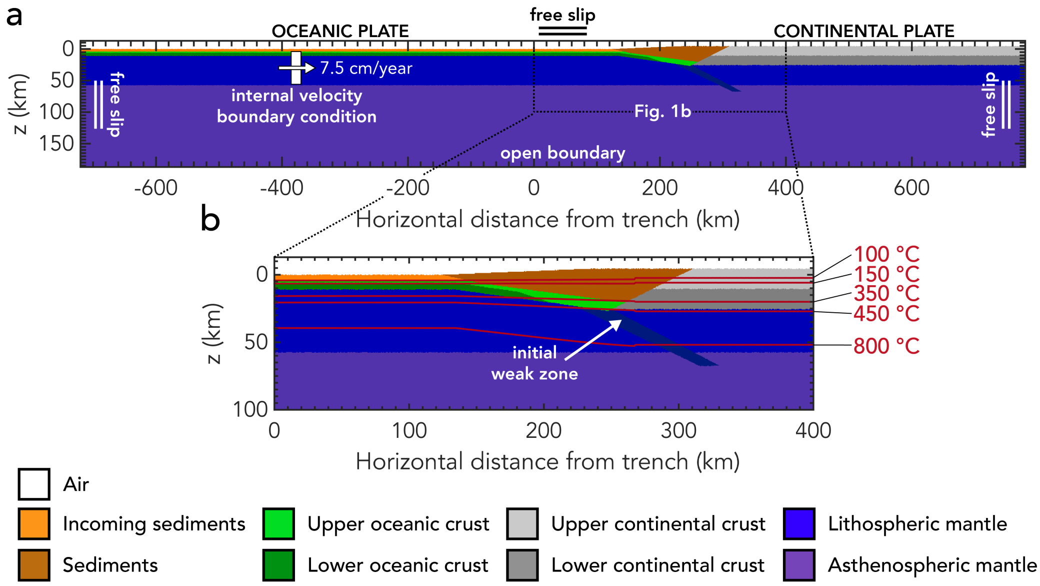

Figure 1. Complete (a) and zoomed (b) model setup of the geodynamic seismic cycle model with lithology (in colour, see key), isotherms (red), and boundary conditions (white). Note that the future trench is located at $(0, 0)$ instead of $(720, 13)$ for easy comparison with the other figures in this work.

2010 M8.8 Maule earthquake. We consider a 1500×200 km^2 box (Fig. 1) with a minimum grid size of 500 m in a high resolution area around the megathrust interface. The high resolution area extends from 0–100 km in the vertical direction and from 650–1225 km in the horizontal direction. In a 50 km region around the high resolution area, we gradually increase the grid size to 2000 m, which is the maximum grid size employed in the rest of the model. This results in a grid of 1654×270 nodes. A total of ~ 54.3 million markers with 20 initial, randomly distributed markers per cell is used to advect the different materials and their physical properties.

The top of the Nazca plate includes a 4 km thick incoming sediment layer to create a large accretionary prism in which splay geometries develop. In addition to the sediment layer, the oceanic Nazca plate consists of a 2 km thick basaltic upper oceanic crust and a 5 km thick gabbroic lower oceanic crust. The initial accretionary wedge consists of sediments and the continental South American plate consists of a 15 km thick sandstone upper continental crust and a 15 km thick sandstone lower continental crust. We use a wet quartzite flow law (Ranalli, 1995) for the continental crust, the sediments, and the upper oceanic crust; and we use a plagioclase flow law (Ranalli, 1995) for the lower oceanic crust. The two plates overlie an anhydrous, peridotitic mantle that is approximated with a dry olivine flow law. We use laboratory-derived material parameters for the different lithology as described in van Dinther, Gerya, Dalguer, Mai, et al. (2013), but update cohesion values constrained by e.g., Ranalli (1995); Schultz (1995), and shear modulus values following Bormann et al. (2012) (Table 2). While these experimental studies typically report a range of plausible values, here we choose either a listed reference value or the value typically used in previous geodynamic modelling studies.

We consider long-term fluid flow with a constant pore fluid pressure ratio. At the start of the model, the ocean floor sediments and oceanic crust contain water.

Regions within 2 km of fluids have an increased pore fluid pressure ratio $\lambda = 0.95$, whereas for dry rocks, the pore fluid pressure ratio $\lambda = 0$. This value of the increased pore fluid pressure ratio is based on observations for Southern Chile (Seno, 2009). The highly over-pressurised pore fluids are primarily required to sustain subduction along a shallow megathrust and obtain reasonable seismic cycle characteristics (van Dinther, Gerya, Dalguer, Mai, et al., 2013). The increased pore fluid pressure ratio results in decreased rock yield stress (Eq. 9). The model does not account for plate (de)hydration reactions for mantle rocks, erosion processes, and serpentinisation.

The seismogenic zone in the SC model develops with the temperature profile of the slab. We impose a velocity-weakening regime when the temperature is higher than 150°C (see Table 2 for lithology-dependent velocity-weakening friction parameters; Blanpied et al., 1995; van Dinther, Gerya, Dalguer, Mai, et al., 2013). Between 100°C and 150°C, there is a transition from velocity-strengthening to velocity-weakening behaviour. The exact switch from velocity-weakening to velocity-strengthening behaviour occurs between the 104°C and 134°C isotherm, depending on rock type and slip rate. We impose a velocity-strengthening regime in the shallow part of the domain when the temperature of the slab is lower than 100°C with the same friction parameters for all rock types with a static friction coefficient $\mu_s^{\mathrm{sc}} = 0.35$ based on sedimentary rocks, a maximum dynamic friction coefficient $\mu_d^{\mathrm{sc}} = 0.875$, and a characteristic slip velocity $V_c = 2 \cdot 10^{-9}$ m/s (see van Dinther, Gerya, Dalguer, Mai, et al., 2013, and references therein for a full derivation of the friction parameters). The downdip limit of the seismogenic zone forms self-consistently due to a brittle-ductile transition that is governed by a decrease in viscosity caused by an increase in temperature.

During the first stage of the model the time step is 1000 years and a suitable subduction geometry is obtained. After 3.6 million years, the time step is gradually reduced to 5 years, which results in the start of the seismic cycle phase of the model after 4.0 million years. We run the seismic cycle phase of the model for ~30 thousand years, during which the stresses are initially adapted to seismic cycles. Then, our long run time ensures that we have a long enough observation time to produce robust seismic cycle statistics (van Dinther, Gerya, Dalguer, Mai, et al., 2013).

We use a sticky air approach to approximate a free surface (Crameri et al., 2012). Free slip boundary conditions are used at the top and sides of the model and we have an open boundary condition at the bottom. An internal velocity boundary condition applied to the subducting slab ensures that subduction is initiated and sustained. The initial and boundary conditions we use are the same as in van Dinther, Gerya, Dalguer, Mai, et al. (2013) and are explained in detail in Appendix A, Appendix B and Fig. 1.

3 Dynamic rupture model

We use the two-dimensional version of the software package SeisSol (`http://www.seissol.org`) to solve for earthquake source dynamics coupled to seismic wave propagation (Dumbser & Käser, 2006; de la Puente et al., 2009; Pelties et al., 2014). SeisSol is specifically suited for handling complex geometries due to the use of unstructured triangular computational meshes.

In the following, we shortly summarise the governing equations and frictional failure criterion. The reader is referred to Dumbser and Käser (2006) for a full description of the numerical method and to de la Puente et al. (2009) for details on the implementation of rupture dynamics as an internal boundary condition in two-dimensional models.

3.1 Governing equations

SeisSol solves the elastic wave equation in a two-dimensional Cartesian coordinate system without external body forces in an isotropic, compressible medium:

$$\rho \frac{\partial \mathbf{v}}{\partial t} = \nabla \cdot \boldsymbol{\sigma} \tag{13}$$

$$\dot{\boldsymbol{\varepsilon}}_e = \frac{1}{2G} \frac{\partial \boldsymbol{\sigma}}{\partial t} - \frac{\lambda_1}{2G} \nabla \cdot \mathbf{v}. \tag{14}$$

Eq. 13 is the equation of motion. The main difference in the conservation of momentum between the SC and DR models (Eqs. 2 and 13) is that the DR model neglects gravity. While gravity is negligible on the short time scales of elastodynamics, gravity may play a role in the SC model by potentially favouring continued slab subduction. Eq. 14 is the constitutive relation derived from Hooke's law that relates the strain rate to stresses for an elastic, isotropic material (compare Eq. 14 to Eq. 6; look at Eq. 1). Since we only consider an elastic medium in the DR model, the elastic strain rate $\dot{\boldsymbol{\varepsilon}}_e$ equals the total strain rate $\dot{\boldsymbol{\varepsilon}} = \frac{1}{2}\left(\nabla \mathbf{v} + \nabla \mathbf{v}^T\right)$ (cf. to Eq. 4). λ_1 and G are the Lamé constants, which determine the Poisson's ratio of the model (Secs. 4.2 and 6.1.1).

To discretise this set of equations in space, SeisSol uses a Discontinuous Galerkin (DG) method with a Godunov upwind flux, which represents the solution as an exact Riemann problem at the discontinuity between element interfaces (Dumbser & Käser, 2006; de la Puente et al., 2009). Due to the use of triangular mesh elements, this approach is particularly suited for the discretisation of complex geometries like shallow dipping subduction zones, topography or bathymetry. For the discretisation in time, SeisSol uses an Arbitrary high-order DERivative (ADER) method (Dumbser & Käser, 2006).

Due to the dissipative behaviour of the numerical upwind flux used in SeisSol, spurious high frequency oscillations are subdued in the vicinity of the fault (de la Puente et al., 2009; Pelties et al., 2014; Wollherr et al., 2018). SeisSol is verified with a wide range of two-dimensional and three-dimensional community benchmarks, including strike-slip, dipping and branching fault geometries, laboratory derived friction laws, as well as heterogeneous on-fault initial stresses and material properties (de la Puente et al., 2009; Pelties et al., 2012, 2014; Wollherr et al., 2018) in line with the SCEC/USGS Dynamic Rupture Code Verification exercises (Harris et al., 2011, 2018).

3.2 Failure criterion and friction formulation

We incorporate frictional failure as an internal boundary condition of the element edges associated with the fault, which is meshed explicitly. This on-fault frictional failure criterion refers to failure along a pre-existing fault typically constrained by laboratory experiments. Fault slip in the DR model is therefore restricted to this fault line in contrast to the SC model where the entire domain is theoretically allowed to slip.

To check the failure criterion, the stress tensor, which consists of the initial stress and any subsequent stress change, is rotated into the fault coordinate system defined by the normal and tangential vectors of each fault point. The DR model compares the absolute shear stress $|\tau|$ on the fault to the fault yield stress $\sigma_{\text{yield}}^{\text{dr}}$:

$$\sigma_{\text{yield}}^{\text{dr}} = c + \mu_s^{\text{dr}} \sigma_n. \tag{15}$$

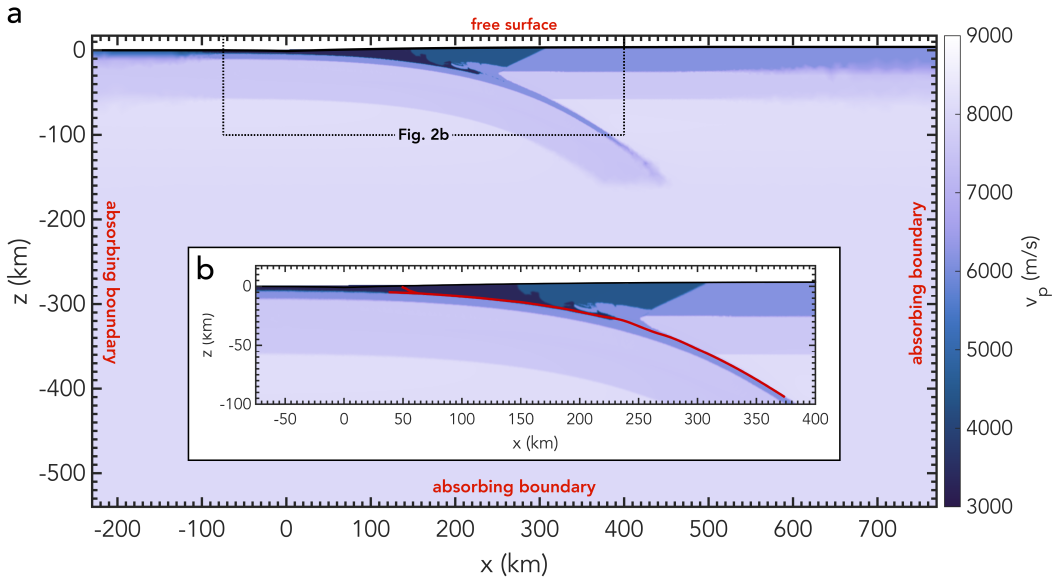

Figure 2. Complete (a) and zoomed (b) model setup of the dynamic rupture model with P–wave velocity v_p (in colour; Table 3), boundary conditions (red) and megathrust and splay fault geometry (red lines). The splay fault is always explicitly meshed in the DR model, but the frictional boundary condition on the splay fault is only activated for the model in Sec. 5.6.

It consists of the fault cohesion c, the static friction coefficient μ_s^{dr}, and the normal stress σ_n (compare to Eq. 9). If the shear stress overcomes the fault's yield stress, the fault fails and its strength becomes $\sigma_{\mathrm{sliding}}^{\mathrm{dr}}$:

$$\sigma_{\mathrm{sliding}}^{\mathrm{dr}} = \mu^{\mathrm{dr}} \sigma_n. \tag{16}$$

During sliding, the friction coefficient μ^{dr} is governed by a linear slip weakening friction law (Ida, 1973). For this constitutive law, μ^{dr} decreases linearly from its static value μ_s^{dr} to its dynamic value μ_d^{dr} with slip distance Δd over a specified critical slip distance D_c, i.e.

$$\mu^{\mathrm{dr}} = \begin{cases} \mu_s^{\mathrm{dr}} - \frac{\mu_s^{\mathrm{dr}} - \mu_d^{\mathrm{dr}}}{D_c} \Delta d & \text{if} \quad \Delta \mathrm{d} < \mathrm{D_c} \\ \mu_d^{\mathrm{dr}} & \text{if} \quad \Delta \mathrm{d} \geq \mathrm{D_c}. \end{cases} \tag{17}$$

Slip produces seismic waves. When failure occurs on the fault, the rupture front and the emitted seismic waves can influence the tractions on the fault. These can bring the fault closer to failure when the normal traction decreases and/or the shear traction increases. It can move the fault further away from failure if the normal traction increases and/or the shear traction decreases.

3.3 Dynamic rupture model setup

The DR modelling domain is a 575 km wide and 169 km deep subsection of the SC domain (Fig. 2). We copy the SC material properties at the boundaries of this domain to extend the DR simulation domain to 1000 km width and 544 km depth to avoid artificial wave reflections from the boundaries. Copying the values is necessary, because of the limited depth of the SC model and the interference of

Table 3. Seismic velocities dynamic rupture model

Material	v_p $\left[\mathrm{m\ s^{-1}}\right]$	v_s $\left[\mathrm{m\ s^{-1}}\right]$
Incoming sediments	3350	1934
Sediments	4429	2557
Upper oceanic crust	6164	3559
Lower oceanic crust	6164	3559
Upper continental crust	6146	3549
Lower continental crust	6146	3549
Lithospheric mantle	7568	4369
Asthenospheric mantle	8090	4671

boundary conditions with the material parameters and physical variables close to the domain edges. The fault geometry is extracted from the SC model according to the region of highest visco-plastic strain rate during the SC coupling event (see Sec. 4.4).

For the dynamic rupture simulations we use a 6^{th} order accurate spatial and temporal discretisation. We use the open source software Gmsh (Geuzaine & Remacle, 2009) to generate the mesh. The nodal grid size at the fault is 200 m and is gradually coarsened to 2.5 km at the edges of a high resolution domain with the same dimensions as the SC subsection domain. Outside this area, we apply rapid coarsening to 50 km at the edges of the larger domain to disseminate the non-perfect absorbing boundary conditions. Note that the fault is additionally subsampled by six Gaussian integration points which increases the resolution on the fault to 33.3 m. The corresponding mesh consists of 543,048 elements.

To ensure stability of the numerical scheme, the time step is calculated in dependence of the Courant-Friedrichs-Lewy criterion using $C_{\mathrm{CFL}} = 0.5$ (de la Puente et al., 2009), the minimum insphere over all mesh elements, and the fastest wave speed v_p. This leads to a time step of $7.5 \cdot 10^{-5}$ s.

Element-wise values for friction parameters, initial stress and yield stress, and rock properties with seismic velocities listed in Table 3, are obtained from the SC model as described in Sec. 4.

We approximate the maximum resolved frequency in our model $f_{\max}$ according to de la Puente et al. (2009):

$$f_{\max} = \frac{v_{\min}}{1.45\Delta x} \tag{18}$$

which is valid for a 4^{th} order discretisation scheme. Here, $v_{\min}$ is the minimum velocity in the model (i.e., the shear velocity of the incoming sediments) and Δx is the grid size. Based on this approximation, the maximum resolved frequency varies from 6.67 Hz on the fault to 0.53 Hz at the edges of the high resolution domain. As we use a 6^{th} order discretisation, we are able to resolve even higher frequencies. These frequencies are well within the range of typical dynamic rupture models (e.g., Wollherr, Gabriel, & Mai, 2019), so our analysis is well resolved.

We use a free surface boundary condition, which sets shear and normal stresses to zero in the absence of external forces. Additionally, the model uses absorbing boundary

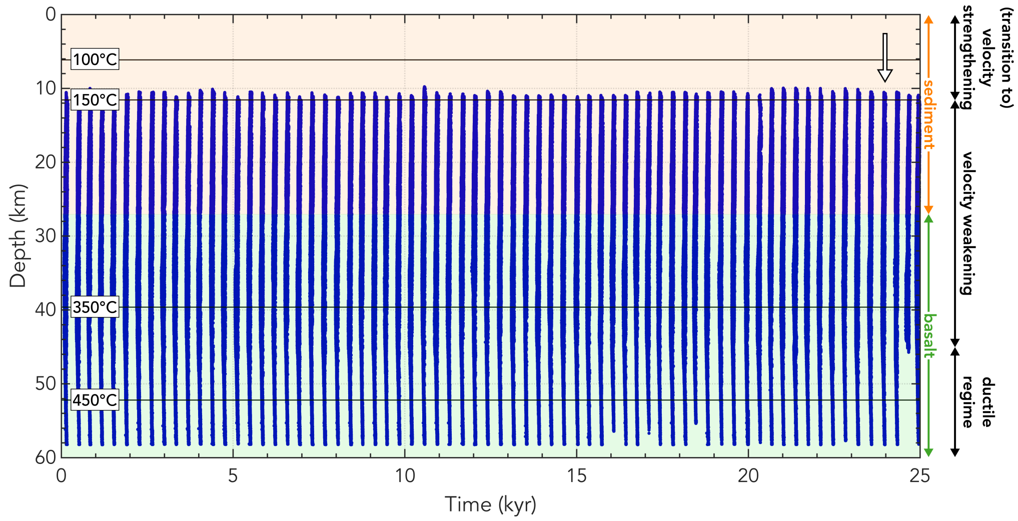

Figure 3. Space-time evolution of the SC model of subduction zone seismicity. Each dot (closely clustered together to form lines) represents a marker that satisfies our Rupture Detector Algorithm thresholds (see text; Dal Zilio et al., 2018). The event that we use as the SC coupling event for our SC to DR coupling is indicated by the arrow. Frictional regimes dependent on temperature are indicated with corresponding isotherms (solid black lines). Background colours represent the rock type through which the fault is going.

conditions that reduce the reflections of outgoing waves at the domain boundaries (Dumbser & Käser, 2006).

4 Coupling method

In this section, we discuss the resulting long-term seismicity characteristics of the SC model and how we choose an event from the SC model to couple to the DR model. We then show how we couple the material properties of the domain, the stresses, the fault geometry, and yield criteria in the two modelling approaches. The full SC results used for coupling to the dynamic rupture model are included as supplementary material and can be used as input for other dynamic rupture models.

4.1 Long-term seismic cycle characteristics and selection of coupling time step

In the seismic cycle phase, we observe 70 spontaneous quasi-periodic megathrust events (Fig. 3). To quantify their characteristics we apply a minimum slip rate threshold of $2.5 \cdot 10^{-9}$ m/s and a minimum stress drop threshold of 0.4 MPa on all markers (Dal Zilio et al., 2018). Most events rupture almost the entire megathrust apart from the shallow, velocity-strengthening part. The exact rupture path is different for each event, because of the different stress and strain distributions for each event in the broad subduction channel and accretionary wedge. This is particularly true in the downdip region of the seismogenic zone where the rupture paths sometimes deviate from the rock interfaces. In the shallow part of the subduction zone, the sediments are favoured over the basalt for rupture propagation, due to their lower yield stress (Table 2). The average recurrence interval of the megathrust events is approximately 270 years, which is in line with estimates of the recurrence interval in Southern Chile (e.g., Cisternas et al., 2005).

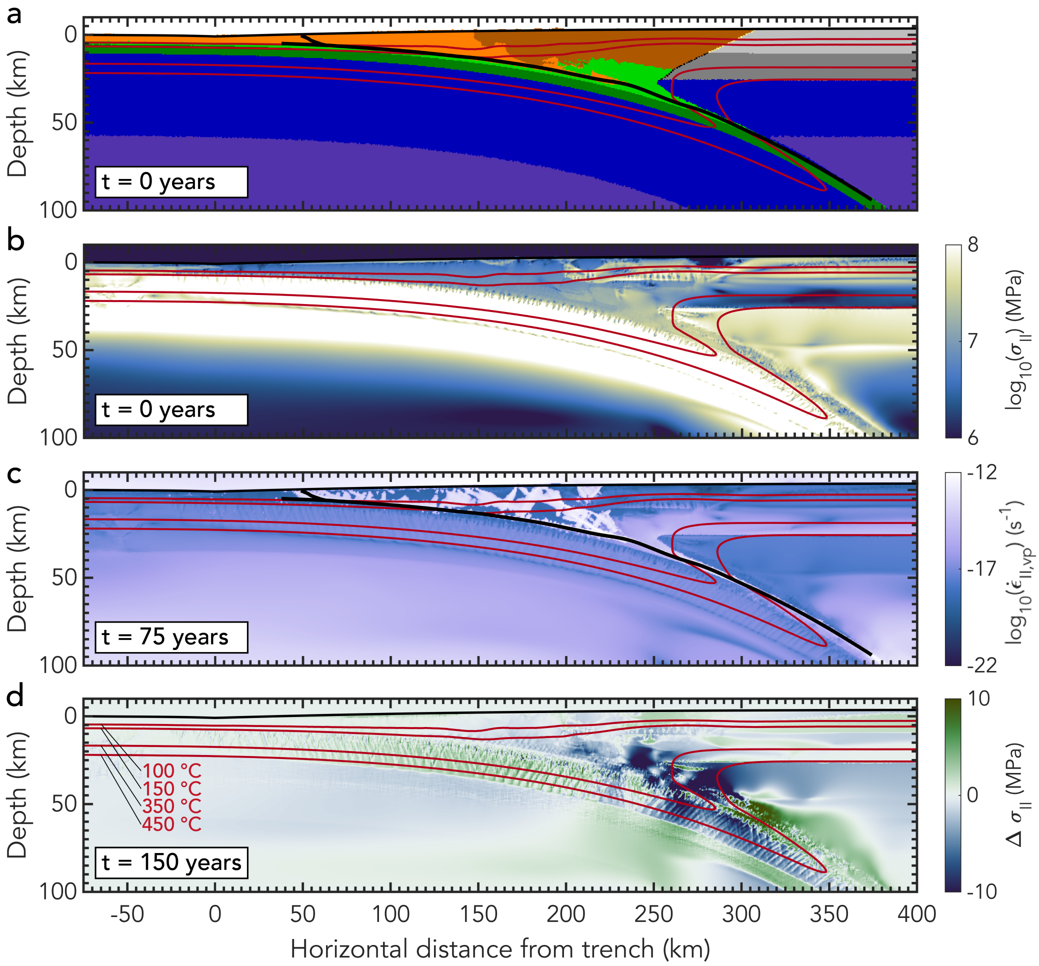

Figure 4. Representative coupling event of the geodynamic seismic cycle model. (a) Lithological structure after 4 Myr (compare to Fig. 1) at the start of the event (t = 0 years) with the fault indicated in black. (b) Initial stress used as input for the DR model. (c) Strain rate during the event at 75 years from the start of the event with the fault indicated in black. (d) Stress change with respect to the initial stress in (b) towards the end of the event 150 years from the start. Isotherms that define the frictional regimes and hence seismogenic zone are indicated in red. The boundary between rocks and sticky air is highlighted with a thick solid black line.

We choose the rupture indicated by the arrow in Fig. 3 as the SC coupling event that we import to the dynamic rupture model. The chosen event is representative for other events in terms of its duration and stress drop and it has a smooth rupture path. The geometry resulting from ~ 4 Myr subduction consists of a large accretionary wedge created by the incoming sediments and a slab with an average dip of 14° (Fig. 4a). At the initiation of the rupture, stress has built up during the interseismic stage in the lower part of the seismogenic zone (Fig. 4b). Like all other events in the SC model, this event also results in a lot of yielding in the shallow part of the accretionary wedge as shown by the strain rate localisation in Fig. 4c. This large yielding region represents the large-scale failure of the unconsolidated accretionary wedge, which contains multiple possible splay fault geometries. Although the localisation of strain on the splay faults and the megathrust is simultaneous, the splay faults are not detected as part of an event, because their lower slip velocity is below the threshold and on the order of $0.1 \cdot 10^{-9}$ m/s to $1 \cdot 10^{-9}$ m/s. The resulting stress change of the SC event in Fig. 4d shows a stress drop in the subduction channel, particularly near the downdip limit of the seismogenic zone.

We need to choose the coupling time step of the SC coupling event for which we import the conditions from the SC model to the DR model as initial conditions. For this coupling time step we export the rock properties, friction coefficient and stresses to the DR model, as discussed in the following sections. We also use this time step as the start of the SC event, so that we can use it and the subsequent time steps that comprise the entire SC event to determine the fault geometry and dynamic friction coefficient.

We select the first time step of the coupling event in the SC model for which nucleation and subsequent propagation of the rupture occur spontaneously in the DR model in order to stay as close to the SC model as possible. This time step corresponds to the time step at which failure occurs in the SC model on two adjacent fault points.

4.2 Lithological structure

Density, shear modulus, and cohesion are directly transported into the DR model. The sticky air material, which is used for the free surface approximation in the SC model, does not enter the DR model, which has a true free surface boundary condition. To provide the DR model with a smooth surface and purely rock-related properties (i.e., no sticky air), we first approximate the air-rock boundary of the SC model with a 3$^{\text{rd}}$ order polynomial that is used as the free surface geometry of the DR model. All parameters, including material properties, stresses, and friction values associated with small sticky air patches residual from the free surface interpolation are then replaced by the corresponding parameters of the underlying rock to prevent any of the sticky air properties to enter the DR model.

The SC model assumes incompressible materials, i.e., Poisson's ratio $\nu = 0.5$. In the DR model, the material is compressible, so $\nu \neq 0.5$. We choose $\nu = 0.25$ to calculate the first Lamé parameter λ_1 from the shear modulus G in the SC model. This value of Poisson's ratio is based on the simplifying assumption that rocks can be treated as Poisson solids with $\lambda_1 = G$ (Stein & Wysession, 2009). We discuss possible variations of Poisson's ratio and its influence on the rupture dynamics in Sec. 6.1.

4.3 Stress state

As the stress in the SC model consists of elastic, viscous, and plastic components, it is important to establish the main deformation mechanism at the coupling time step before transporting the stresses to the fully elastic DR model. We analyse the visco-elasticity factor F at the coupling time step to determine the dominant deformation mechanism (Appendix C). We find that the deformation mechanism in the seismogenic zone (i.e., between temperatures of 150°C and 350°C) of the SC model is elastic behaviour, which results in stresses with an almost purely elastic component (i.e, $F < 0.05$; Appendix C; Fig. C1). At temperatures higher than 350°C, the deformation mechanism in the subduction channel slowly starts to include a viscous component as a result of dislocation creep. This change in deformation mechanism effectively defines the downdip limit of the seismogenic zone.

Hence, we mainly transport elastic stresses from the visco-elasto-plastic SC model to the elastic DR model in the seismogenic zone. Exporting the stresses from the SC model to the DR model ensures that the stress history from the SC model is preserved in the DR model on the fault. The stresses then continue to evolve during the dynamic rupture in the DR model.

The SC model uses deviatoric stresses σ', like many other geodynamic models, whereas the DR model uses non-deviatoric stresses. The two models also use different sign and coordinate conventions (more details in the Supporting Information), so the stresses from the SC model need to be converted to the conventions of the DR model.

First, the deviatoric stresses σ'^{sc} of the SC model are converted to non-deviatoric stresses σ^{sc} according to

$$\sigma^{sc} = \begin{pmatrix} \sigma^{sc}_{xx} & \sigma^{sc}_{xz} \\ \sigma^{sc}_{xz} & \sigma^{sc}_{zz} \end{pmatrix} = \begin{pmatrix} \sigma'^{sc}_{xx} - P & \sigma^{sc}_{xz} \\ \sigma^{sc}_{xz} & -\sigma'^{sc}_{xx} - P \end{pmatrix}, \tag{19}$$

where P is the solid rock pressure.

Besides that, we need to take into account the different coordinate systems with the z-axis pointing downwards for the SC model and upwards for the DR model. The two models also have opposite stress conventions for both the diagonal and shear components of the stress tensor (see the Supporting Information for details). To account for this, we use the following stress tensor as input for the DR model:

$$\sigma^{dr} = \begin{pmatrix} -\sigma^{sc}_{xx} & \sigma^{sc}_{xz} \\ \sigma^{sc}_{xz} & -\sigma^{sc}_{zz} \end{pmatrix}. \tag{20}$$

We use bilinear interpolation to map the SC stress field from the regular SC grid onto the sub-elemental Gaussian integration points along the edges of all triangular elements holding a dynamic rupture boundary condition. Based on the fault orientation, the shear and normal tractions on the fault are then determined to evaluate the yield criterion in the DR model (Eq. 15).

4.4 Fault geometry

In the SC model we use Drucker-Prager plasticity to approximate the brittle failure in a continuous medium (Eq. 9). Plastic yielding of the SC model manifests itself in the localisation of strain rate in shear bands, which we interpret as faults. Therefore, the SC model has no pre-defined, discontinuous fault surfaces to which fault slip is explicitly restricted. Instead, fault orientations are determined by the local stress field (Preuss et al., 2019) and fault slip rate and slip are calculated from local, visco-plastic strain rates assuming one grid cell wide faults (e.g., van Dinther, Gerya, Dalguer, Mai, et al., 2013). In contrast, the DR model uses the elastic Coulomb criterion (Eq. 14) to describe failure on pre-existing, infinitely thin, discontinuous fault interfaces.

As the fault geometry in the DR model needs to be predefined, we have to define a localised, infinitely thin fault line from the SC model. Therefore, we look at the

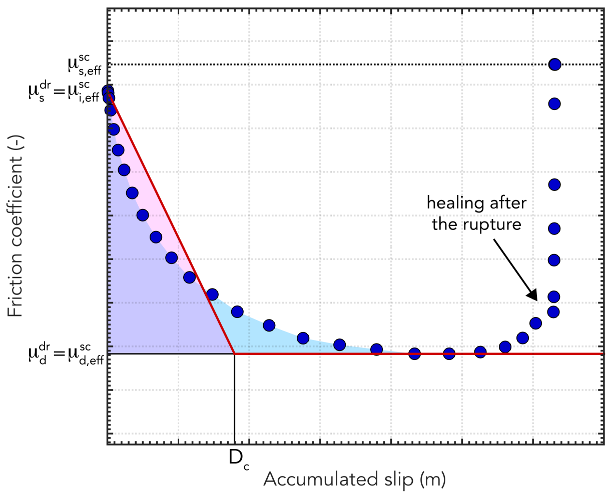

Figure 5. Illustration of the linear slip weakening approximation of rate-dependent friction for one fault point. Each blue dot represents the effective friction coefficient and corresponding accumulated slip for one time step of the SC model during the entire rupture. The final picked μ_s^{dr}, μ_d^{dr}, and D_c are indicated by solid black lines. The final linear slip weakening approximation is indicated in red. D_c is calculated by ensuring that the friction drop during slip of the linear slip weakening law (pink area underneath red line) equals the friction drop during slip of the rate-dependent friction law (blue area underneath blue dots). The area is purple where these two areas overlap. Note that the static friction coefficient of the DR model is not necessarily equal to that of the SC model, but instead equals the SC friction coefficient at the start of the event $\mu_{i,\mathrm{eff}}^{\mathrm{sc}}$.

coupling time step of Sec. 4.1 and the 43 subsequent time steps that make up the SC event. We pick the z-coordinate with the highest visco-plastic strain rate during the entire SC slip event for each nodal x-coordinate (Fig. 4c). We smooth the fault with a moving average low-pass filter scheme with a span of 25 points to avoid stair-casing effects due to the rectangular discretisation and low resolution of the SC model. This ensures that the nucleation region is correctly represented in the fault geometry.

The SC fault geometry reveals that a shallow splay fault is preferred over the megathrust in the velocity-strengthening region (Figs. 2 and 4). For simplicity, our models initially only contain the megathrust, which is manually extended by adding $\sim$ 25 km updip of the fault with the constant dip from the shallowest part of the megathrust. The total length of the megathrust is then 351.3 km with an average dip of 14.3° and a minimum and maximum dip of 2.3° and 34.4°, respectively. The splay fault is connected to the megathrust at x = 24.5 km along the megathrust. It has a length of 14.6 km with an average dip of 21.1° and a minimum and maximum dip of 8.1° and 36.8°, respectively. This splay fault is included in the mesh for all DR models to ensure that the results of adding a splay fault in Sec. 5.6 are not influenced by any changes in the mesh. In Sec. 5.6, the frictional boundary condition on the splay fault is activated, so that slip on the splay fault is theoretically possible. In all other models, the frictional boundary condition on the splay fault is turned off.

4.5 Yield criteria

Yielding and slip in the SC and DR models are governed by different physical mechanisms. The static friction in the SC model is an internal friction coefficient that is a material property inherent to the host rock, whereas the static friction coefficient in the DR model is a frictional property assigned only to the fault. However, internal and on-fault friction coefficients have the same range of possible values (e.g., Tables 9.5 and 9.7 in Pollard & Fletcher, 2005) and may be assumed to be equal (e.g., Gabriel et al., 2013). We also assume that the bulk cohesion C in the SC model is equal to the on-fault cohesion c in the DR model.

We translate the SC yield criterion to the DR model by equating Eqs. 9 and 15. We observe an average difference of 7 MPa between SC pressure and DR normal tractions, which is negligible compared to their absolute magnitudes in the range of gigapascals. Assuming that the magnitude of the pressure or mean stress P, is equal to the magnitude of the effective normal traction, σ_n, leads to the following relationship between the friction coefficients

$$\mu^{\mathrm{dr}} = \mu^{\mathrm{sc}}_{\mathrm{eff}} = (1-\lambda)\mu^{\mathrm{sc}}. \tag{21}$$

Hence, the presence of pore fluids, with a pore fluid pressure ratio $\lambda = 0.95$, reduces the effective friction coefficient in the SC model (Sec. 2.4). An advantage of this coupling is that the on-fault friction coefficients vary in dependance of rock type throughout the DR model. The effective friction coefficients range from 0.028 to 0.005 and are in line with theoretical estimates (e.g., Wang & Hu, 2006) and experiments (e.g., Kopf & Brown, 2003; Ujiie et al., 2013). We import the current friction coefficient μ^{sc}_i of our coupling time step as the initial, static friction coefficient for the DR model. We use the minimum friction coefficient μ^{sc}_d that is reached during the event in the SC model as the DR dynamic friction coefficient. The corresponding characteristic slip distance D_c is then calculated such that the area of the strength drop during slip of the linear slip weakening law equals the area of the strength drop during slip of the rate-dependent friction law:

$$D_c = \frac{2}{\mu^{\mathrm{dr}}_s - \mu^{\mathrm{dr}}_d} \sum_{t=1}^{t_{\max}} \Big(d_t - d_{t-1}\Big) \cdot \Big(\mu^{\mathrm{sc}}_{\mathrm{eff},t} + \frac{1}{2}\mu^{\mathrm{sc}}_{\mathrm{eff},t-1} - \mu^{\mathrm{dr}}_d\Big). \tag{22}$$

Here, $t = 0$ is the coupling time step (Sec. 4.1), $t_{\max}$ is the time step in the SC model at which the lowest friction coefficient is obtained, d is the accumulated slip for a given point in time and the SC friction coefficients are the effective friction coefficients. Also note that $\mu^{\mathrm{dr}}_d = \mu^{\mathrm{sc}}_{d,\mathrm{eff}}$. Fig. 5 illustrates this friction law approximation for one fault point, with the data from the SC model plotted as blue dots and the corresponding linear slip weakening approximation for the DR model in red.

Using this approach, we get a self-consistent approximation in the DR model of the velocity-strengthening behaviour in the shallow part of the SC model by having $\mu^{\mathrm{dr}}_d > \mu^{\mathrm{dr}}_s$.

We use the same bilinear interpolation scheme used for the SC stress field to map the friction coefficients and the cohesion onto the DR fault.

5 Results and analysis

In this section, we first describe the on-fault stress state that results from the SC model in Sec. 5.1. We then describe the results from the SC event (Sec. 5.2) and the corresponding DR rupture (Sec. 5.3) in detail and compare them (Sec. 5.4). In Sec. 5.5, we study the effect of complex lithological structures on the resulting rupture through a series of increasingly complex models studies. Lastly, we analyse how a splay fault affects the dynamic rupture in Sec. 5.6.

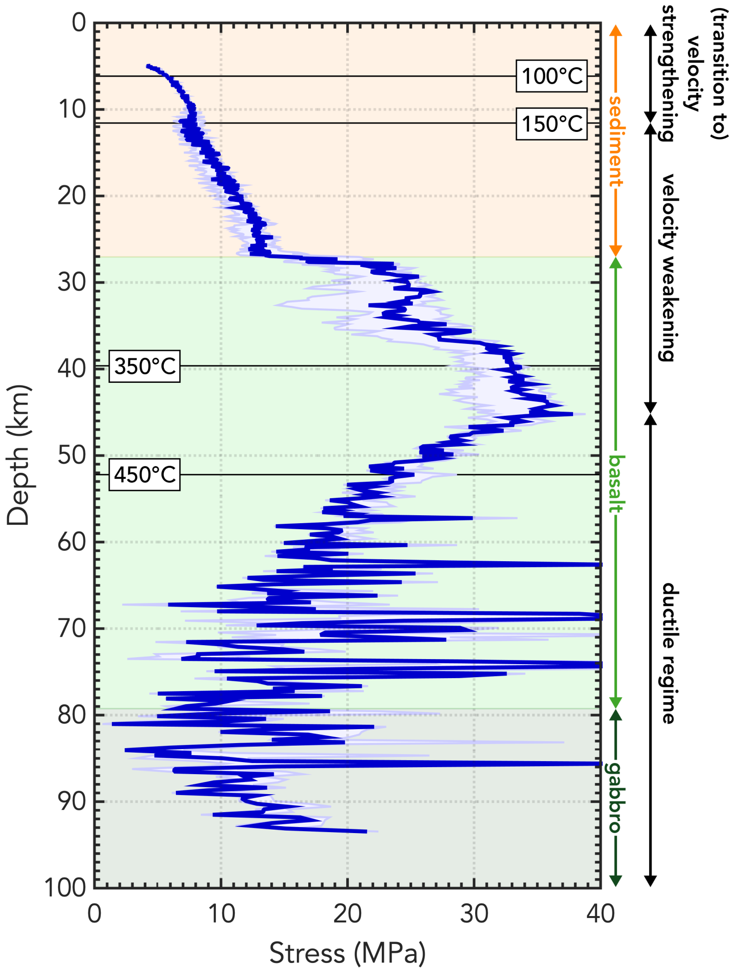

Figure 6. Variability of the stress σ'_{II} at the time of nucleation indicated by the light blue shaded area with the initial stress of the reference model indicated by the blue line. Frictional regimes dependent on temperature are indicated with corresponding isotherms (solid black lines). Background colours represent the rock type through which the fault is going.

5.1 Long-term constrained stress state of the megathrust

Fig. 6 shows the variability of the on-fault stress σ'_{II} which is used in the SC failure criterion (Eqs. 7 and 9) for the 14 events during the last 5000 years of simulation time of the SC model. It is calculated by obtaining the minimum and maximum stress for each fault point from 10 time steps around the nucleation time. For simplicity, we used the fault geometry of the coupled SC event (Sec. 4.4), although the actual fault geometries of other events might deviate from that of the coupled event (van Dinther, Gerya, Dalguer, Mai, et al., 2013). We visualise variables of the SC model on the discrete DR fault (Sec. 4.4) by using the values of the neighbouring grid cell with the highest strain rate for each fault point, which approximates the fault of the SC event optimally. As the rupture path changes for each event, this leads to slight deviations in individual stress profiles, but it does not change the overall stress variability, i.e., the minimum and maximum possible initial stress at a fault point.

The stress profiles in Fig. 6 all show a similar trend in terms of stress distribution along the fault with depth and the amount of stress heterogeneity. There is no

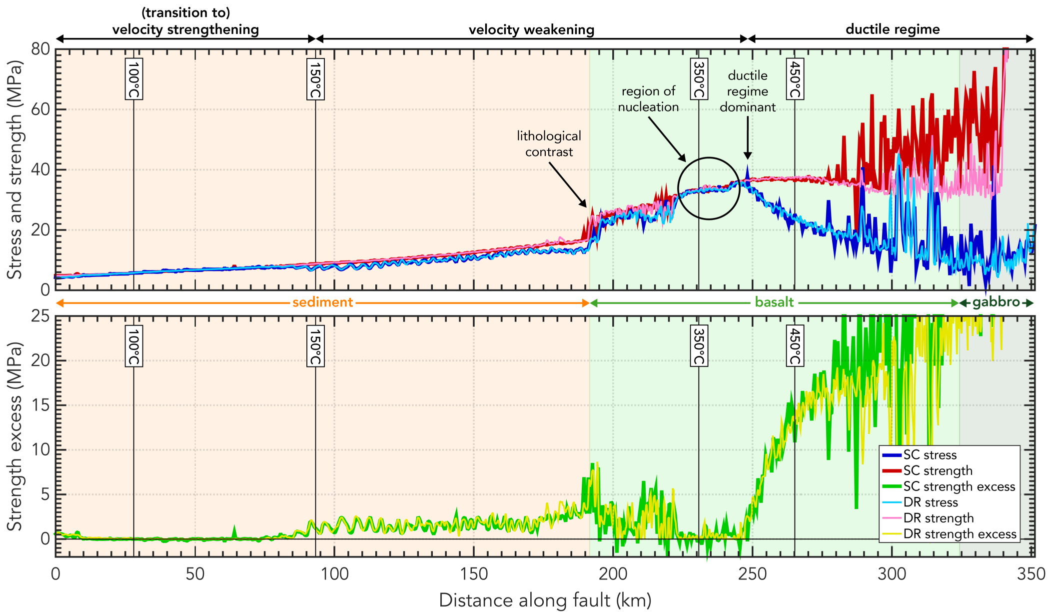

Figure 7. Failure analysis of the SC model at the coupling time step and thus the initial conditions of the DR model along the fault. Second invariant of the deviatoric stress tensor σ'_{II}, yield stress $\sigma^{\mathrm{sc}}_{\mathrm{yield}}$, and strength excess $\sigma^{\mathrm{sc}}_{\mathrm{yield}} - \sigma'_{II}$ for the SC model (bold lines); and initial shear stress τ, fault yield stress $\sigma^{\mathrm{dr}}_{\mathrm{yield}}$, and strength excess $\sigma^{\mathrm{dr}}_{\mathrm{yield}} - \tau$ for the DR model (thin lines) in the fault coordinate system. Frictional regimes dependent on temperature are indicated with corresponding isotherms (solid black lines). Background colours represent the material through which the fault is going.

stress variability in the upper part of the sediments where the velocity-strengthening regime dominates. This is due to the fact that the events do not propagate on this part of the fault, but instead choose a splay fault over the megathrust in the velocity-strengthening region (Sec. 4.4). There is little variation in the velocity-weakening regime of the sediments. There is no sharp transition between sediments and basalt, but instead the two materials are intermixed. This results in a high stress variability in the shallow part of the basaltic region indicated in Fig. 6. The stress variability becomes larger in the basalt with the maximum difference in nucleation stress at a given fault point being 11.5 MPa. There is a peak in the stresses at the downdip end of the seismogenic zone below the 350°C isotherm. This is the nucleation region of most of the SC events. Here, the stress build-up is the largest, because the differential displacement between the locked seismogenic zone and the creeping viscous domain is the largest. In the ductile regime starting at 45 km depth, the stresses decrease by viscous relaxation related to the dislocation creep (Fig. 6). The spontaneous brittle-ductile transition occurs, because the viscosity of the materials gradually decreases by several orders of magnitude due to an increase in temperature with depth (Eq. 8). The exact location of the transition is governed by the laboratory-derived viscous parameters in the wet quartzite flow law (Table 2). In the ductile regime, the stress variability between events is small, but all stress fields show the same highly heterogeneous behaviour. These stress heterogeneities are mainly caused by the close proximity and intermittent presence of mixed pockets of basalt, gabbro and mantle. These lithologies have different viscous flow law parameters and thus have a different viscosity for the same temperature and pressure conditions. This leads to distinct differences in stress build-up and relaxation, which causes a highly heterogeneous stress state.

Fig. 7 focuses on the stress and strength conditions for the coupled event to analyse where failure is occurring in each of the models. According to their failure criterion, the SC model compares the initial second invariant of the deviatoric stress tensor σ'_{II} with the yield stress $\sigma^{\mathrm{sc}}_{\mathrm{yield}}$ of the rock, whereas the DR model compares the initial shear stress τ to the fault yield stress $\sigma^{\mathrm{dr}}_{\mathrm{yield}}$. In the following sections, the term "stress" is generally used to refer to both σ'_{II} and τ, and "yield stress" is used to refer to $\sigma^{\mathrm{sc}}_{\mathrm{yield}}$ and $\sigma^{\mathrm{dr}}_{\mathrm{yield}}$.

The values for the second invariant of the deviatoric stress $\sigma'_{II} = \sqrt{\sigma'^2_{xx} + \sigma'^2_{xz}}$ in the SC model range from 1.4 MPa to 37.8 MPa. In the shallow part of the fault, where the fault is embedded in the sediments of the accretionary wedge, the stress and yield stress are close, which reflects the constant closeness to failure of creeping patches during the interseismic period. The proximity of sediments and basalt in the subduction channel results in a material change on the fault with a corresponding stress and yield stress change, as these two materials have different elastic moduli, friction and cohesion values (Fig. 4 and Table 2). The stress and yield stress variability between 192 and 223 km along the fault is large, because there are isolated patches of subducted sediments in the basalt close to the fault that locally affect the stress and yield stress on the fault. The nucleation region is located in the basaltic region near the down-dip limit of the seismogenic zone. For the chosen coupling time step from the SC model, stress reaches the yield stress of the basalt at the nucleation region $\sim$ 225–245 km along the fault. The peak stress in the basalt reaches 37.8 MPa. The stresses drop when the viscous behaviour becomes dominant at 248 km along the fault. The material change from basalt to gabbro is not accompanied by a distinct change in stress or yield stress. This is because the frictional properties no longer dictate the stress and yield stress of the rock in the ductile regime. The oscillations of the stress and yield stress in the ductile regime are caused by material heterogeneity. Smaller oscillations, as observed in the sediment and basalt are due to mapping the SC properties onto the discrete DR fault with the nearest neighbour interpolation.

5.2 Geodynamic seismic cycle slip event

Fig. 8 shows the on-fault evolution of slip rate during both the SC and DR events through space and time. Important features are indicated by numbers, which are discussed in this and the following section.

The slip rate of the SC model in Fig. 8a shows the initial nucleation phase indicated by (1) during which slip rates are still low $V < 1.0 \cdot 10^{-9}$ m/s. After $\sim$ 50 years, the rupture starts propagating mainly updip until it is stalled when entering the velocity-strengthening region (2) and the ductile regime (3). The highest slip rates of $5.7 \cdot 10^{-9}$ m/s are reached in the sediments. There is continuous creep on the fault in the ductile regime with slip rates of $\sim 3 \cdot 10^{-10}$ m/s. The SC event lasts for 180 years due to the 5 year time step and the low characteristic velocity in the slip rate-dependent friction formulation. The low slip rate during the rupture on the order of 10^{-9} m/s is a direct result of this. Note that due to the evaluation of this event with the nearest neighbour interpolation at the fault geometry approximation adopted for the DR model, we see visual artefacts in the form of stripes (4) in Figs. 8a,b. Similar artefacts are introduced in the DR coupling by the interpolation of the coarse SC model resolution variables onto the high resolution DR fault.

The corresponding stress change along the fault with respect to the initial stress of the event over time always shows a stress increase (1) ahead of the rupture front due to the conservation of momentum (Fig. 8b). We observe a maximum stress drop over time of 15 MPa in the nucleation region. The stress drop is material dependent, as the stress drop in the basalt is 9.4 MPa on average, whereas the average stress drop of the sediments is 2.8 MPa. We find an average stress drop of 5.6 MPa between the 150°C

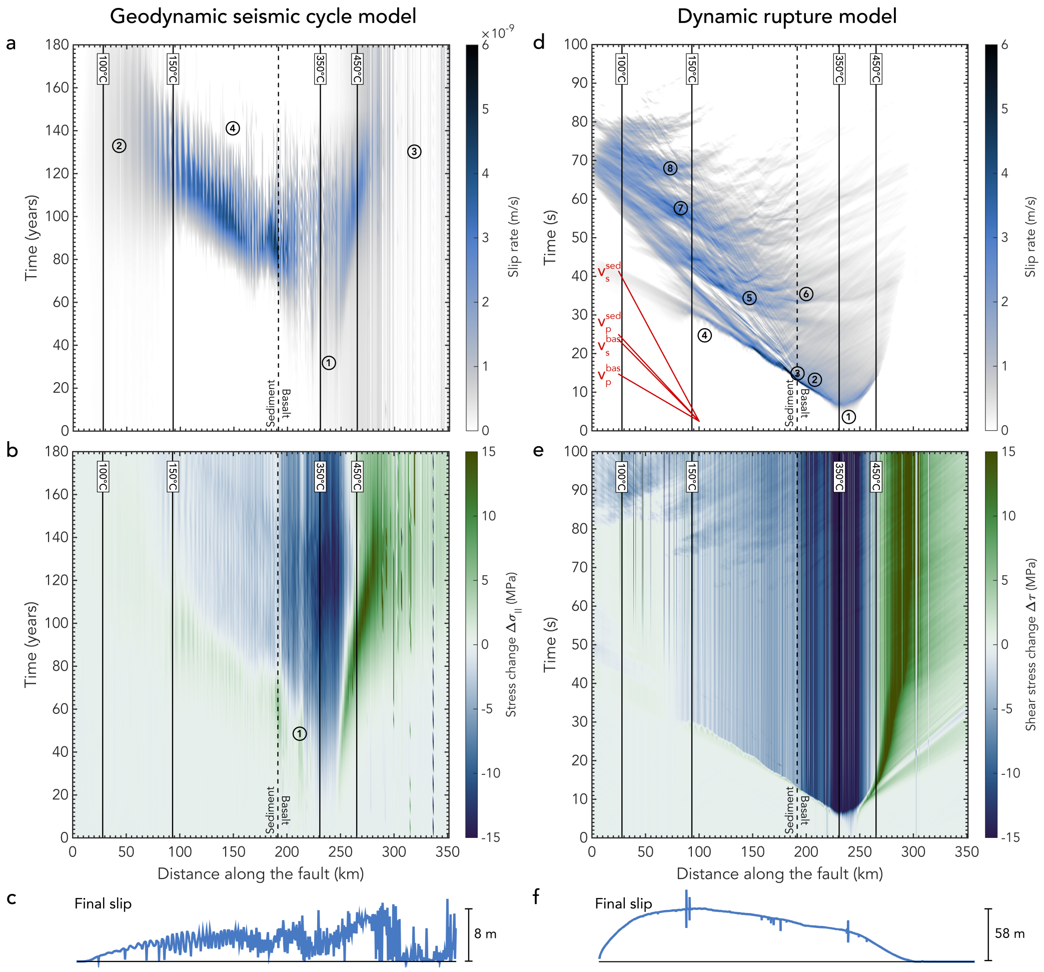

Figure 8. Slip rate evolution with time (a,d), temporal stress change evolution (b,e), and final accumulated slip (c,f) along the fault for the same rupture in the SC model (left column) and the DR model (right column). Solid lines indicate the isotherms that define the frictional regimes; dotted line indicates material change. The P- and S-wave velocities v_p and v_s for both the basalt ($_{\text{bas}}$) and sediment ($_{\text{sed}}$) are indicated in red. Numbers are discussed in the text. We take $t = 0$ years in the SC model for the time step at which we transfer the stresses. The oscillating behaviour visible in the SC final slip distribution stems from the visualisation of the interpolation of the continuous SC model on the discrete DR fault. Low slip rates and high stress drop near the nucleation region likely show the approximated fault does not capture the main slip patch there. Peak slip is indicated.

and 450°C isotherms. When the frictional regime transitions from velocity-weakening to velocity-strengthening at the updip limit of the seismogenic zone, the stress drop becomes very small.

The final slip distribution in Fig. 8c shows high slip with a maximum of 8.3 m in the deeper part of the seismogenic zone, which decreases towards the trench and the ductile regime. Note that slip below the 450°C isotherm is largely the result of continuous, ductile creep.

5.3 Coupled dynamic rupture event

The initial conditions imported from the SC model result in the spontaneous nucleation of an earthquake within the DR model (Fig. 8d, (1)) without using any artificial nucleation procedures. The nucleation phase before the spontaneous rupture propagation lasts for $\sim$ 6.5 s and results in a large nucleation patch of $\sim$ 27 km between $x = 222$ km and $x = 249$ km along the fault. In the DR model, failure also occurs immediately between $x = 10$ km and $x = 75$ km, which are the regions where shallow interseismic creep is seen in the SC model (Fig. 7). This instantaneous failure does not lead to the nucleation of a large earthquake, but does emit seismic waves. The associated stress drops are on the order of $\sim$ 0.1 MPa and thus low compared to the stress drop of the main rupture. The friction increases slightly in the velocity-strengthening sediments from its static value of 0.0176 to a dynamic value of 0.0177. Slip rates of 0.08 m/s are reached locally and accumulate 0.04 m of slip. We do not observe pronounced interaction of the instantaneously emitted waves with the down-dip nucleating spontaneous rupture event. Importantly, the DR instantaneous failure of the SC creeping sections leaves behind a heterogeneous initial stress configuration close to, but not at, failure (S parameter $\sim$ 0.01 after the initial stress drops, see Appendix D). These fault sections are readily re-activated by the main rupture later on. Another considerable instantaneous stress drop of $\sim$ 4.0 MPa occurs between $x = 219$ km and $x = 222$ km along the fault. Although this stress drop is also low compared to the stress drop of the main rupture, the downwards travelling emitted seismic waves do interact with the upward travelling main rupture front. However, the associated mean slip rate of 0.0022 m/s and slip of 0.05 m are low compared to the main rupture.

After the nucleation phase, the rupture mainly propagates updip. There is spontaneous rupture arrest below the downdip limit of the seismogenic zone 290–300 km along the fault. In the basalt, supershear rupture speeds of $\sim$ 6100 m/s ($v_p = 6164$ m/s; $v_s = 3559$ m/s) are reached at the onset of rupture. These speeds are promoted by a low S parameter of 0–0.5 (e.g., Gabriel et al., 2012), which is defined as the ratio between initial strength excess and nominal stress drop (Das and Aki (1977b); Appendix D). Closely spaced secondary non-supershear rupture fronts (2) follow this main supershear rupture front. The rupture velocities change when the rupture enters the lower seismic velocity sediments (3). The main rupture front propagates updip at supershear velocities of $\sim$ 3340 m/s ($v_p = 3350$ m/s; $v_s = 1934$ m/s), and the second rupture fronts travel at speeds of $\sim$ 1750 m/s in the sediment close to its Rayleigh speed. The change in material, and hence seismic velocities, also results in an impedance contrast, which causes the reactivation of fault slip due to reflected seismic waves from the sediment–basalt transition (3). Rupture propagation in the sediments in the shallow part of the megathrust features small scale failure preceding the main rupture front arrival (4). These phases have slip rates of $\sim$ 0.5 m/s and their rupture speeds are low with 1700 m/s. Their occurrence is promoted by (*i*) a very low strength excess of 1.0 MPa; and (*ii*) on-fault, dynamic stress accumulation preceding the main rupture front. These localised precursory phases do not merge into a combined rupture front but are overtaken by the faster main rupture.

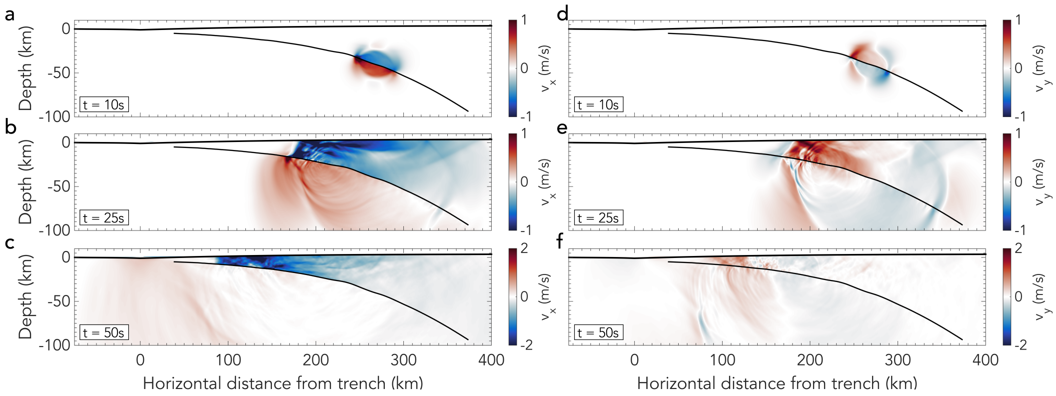

Figure 9. Horizontal (a,b,c) and vertical (d,e,f) velocity in the DR coupling model of Sec. 5.3 at $t = 10$ s, $t = 25$ s and $t = 50$ s. Fault is indicated in black.

The rupture is predominantly crack-like, although pulse-like behaviour is observed in the sediments. Crack-like rupture behaviour is characterised by continuous slip on the fault after arrival of the rupture front (Kostrov, 1964). During a pulse-like rupture, slip on the fault only occurs for a relatively small amount of time after the arrival of the rupture front compared to the entire duration of the rupture (Brune, 1970).

Surface reflections at (5) provide additional energy to the rupture, which results in the breaking of the shallow megathrust. This is in line with similar behaviour found by Kozdon and Dunham (2013) for dynamic rupture models of the 2011 Tōhoku-Oki earthquake. Waves are also reflected at the material contrast between sediments and basalt at (6). Later surface reflections at (7) and (8) reactivate the downdip part of the megathrust. The highest slip rate values of 10.9 m/s are reached as the rupture tip reaches the sediment-basalt transition.

The stress drop in Fig. 8e, calculated as the stress change with respect to the initial stress, is material dependent, with large stress drops of 14 MPa in the basalt and 5.3 MPa in the sediments. The average stress drop between the 150°C and 450°C isotherms is 9.3 MPa. Initially, there is little stress drop in the velocity-strengthening region at the updip limit of the seismogenic zone. However, after ~ 70 s, the stresses drop in the sediments, even though fault slip has stopped. This could be due to (i) dynamic on-fault stress transfers caused by healing fronts of the rupture pulses (e.g., Nielsen & Madariaga, 2003; Gabriel et al., 2012), or (ii) dynamically triggered reactivation of the fault by the seismic waves (e.g., Belardinelli et al., 2003).

The corresponding final slip distribution in Fig. 8f shows that the maximum slip of 57.9 m (disregarding the unphysical isolated peaks) occurs in the sediments, at the frictional updip limit of the seismogenic zone. Slip tapers off towards the trench and the downdip limit of the seismogenic zone.

Fig. 9 visualises the wave field at several time steps. At 10 s the rupture has nucleated completely (also see Fig. 8d) and the wave field looks relatively simple. After 25 s, complex interactions between the free surface and the emitted waves are visible. Most notably, a large reflected wave is travelling towards the fault. After 50 s most of the waves are trapped in the accretionary wedge. This results in continuous reactivation of the fault slip which highly increases the slip in the shallow part of the fault.

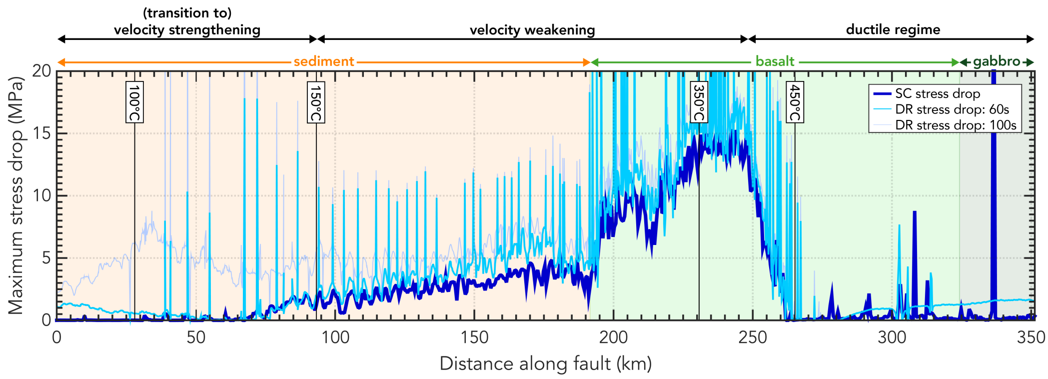

Figure 10. Maximum stress drop in the SC model and DR model (after the first 60 s and at the end of the event at 100 s) along the fault. The peaks of high stress drop in the DR model responsible for the stripes in Fig. 8e are directly related to the input from the SC model. Since the resolution in the DR model is higher, isolated fault points get affected by the interpolation of the coarser model input from the SC model. Frictional regimes dependent on temperature are indicated with corresponding isotherms (solid black lines). Background colours represent the material through which the fault is going.

5.4 Comparison of events in the seismic cycle and dynamic rupture models

Both events nucleate in the same location, which demonstrates the successful coupling of fault stress and strength conditions (Fig. 7 and 8). These coupled initial conditions then affect the full dynamic rupture behaviour. Most notably, they cause spontaneous rupture arrest at depth ($z = 65$ km) in the DR model due to the increase of strength excess when the deformation mechanism changes from brittle to ductile in the SC model (Sec. 5.1).

Using the stress and yield stress of the SC model as input for the DR model results in material dependent stress drop in the DR model. Prior to slip reactivation due to wave reflections, the stress drop values and distribution of the DR event are similar to those of the SC event (Fig. 10). In the nucleation region the stress drop is on the order of $\sim$ 14 MPa. After 60 s of rupture, the stress drop in the DR model increases due to reactivation of rupture due to the reflected seismic waves that are not present in the SC model. Therefore, the DR model shows higher final stress drops in the sediments than in the SC model. The similarity of the stress drops between the models before the reactivation of fault slip in the DR model demonstrates the successful coupling of the two codes even though their friction behaviour is described by different laws (secs. 2.3 and 3.2).

The slip distribution and absolute values of the SC and DR model are different, since the DR model additionally resolves the emitted seismic waves that reactivate fault slip and uses a lower Poisson's ratio. The contributions of the reflected waves and Poisson's ratio on fault slip are explored in Secs. 5.5 and 6.1.1.

In summary, the SC and DR rupture are qualitatively comparable in terms of rupture nucleation, propagation, and arrest. They are also quantitatively comparable in terms of stress drop. However, the amount of slip is significantly larger in the DR model.

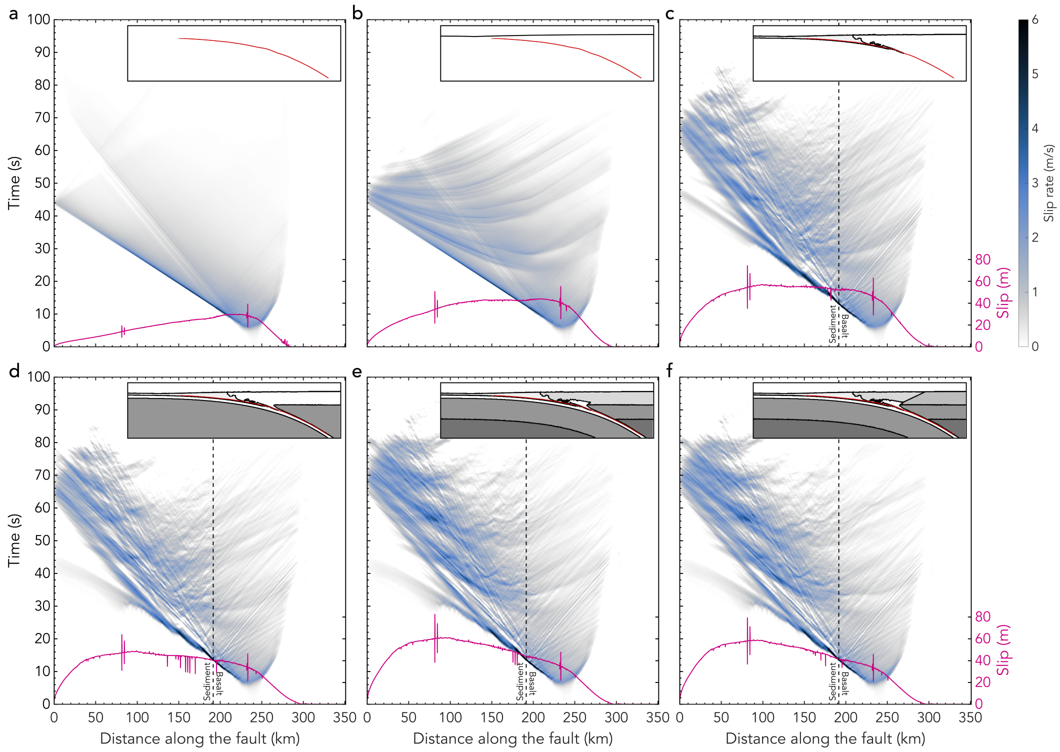

Figure 11. Slip rate evolution of a megathrust rupture for (a) a homogeneous model with basaltic composition and an extended top boundary to exclude any interactions of the seismic waves with the free surface; (b) a homogeneous model with basaltic composition including the free surface as the top boundary condition; (c) the model of Fig. 11b with the addition of incoming sediments; (d) the model of Fig. 11c with the addition of lithospheric mantle; (e) the model of Fig. 11d with the addition of asthenospheric mantle and accretionary wedge sediments; (f) the model of Fig. 11e with the addition of continental crust. Insets show the lithological structure (grey scale colours) and impedance contrasts (black) (Fig. 4a). Dotted line indicates material change between basalt and sediments. Pink lines show the final slip distribution on the fault.

5.5 The role of complex lithological structures

A common simplification in many dynamic rupture studies is the use of homogeneous material and friction parameters (e.g., Ma, 2012; Huang et al., 2013). However, in models that include material contrasts, particularly close to the fault, it has been shown that lithological structures affect the rupture (e.g., Huang et al., 2014; Pelties et al., 2015; Lotto et al., 2017). Lithological structures refer to large scale rock or material variations with different properties. Waves reflecting of lithological contrasts are governed by the impedance contrast between rock types. Seismic impedance Z is defined as seismic wave velocity times density ($Z = v \cdot \rho$, see Tables 2 and 3 for values). Large impedance contrasts favour wave reflection, whereas no or small impedance contrasts favour wave transmission. The reflected waves can impact the fault again which affects the on-fault stress field and thereby the rupture dynamics. For example, the resulting on-fault stress changes can lead to the (re-)activation of fault slip and alter the rupture speed (Sec. 5.3; Kozdon & Dunham, 2013; Huang et al., 2014; Pelties et al., 2015).

The SC model provides a complex geometry with temperature-dependent elastic properties for the DR model, which results from millions of years of thermo-mechanically coupled subduction. We systematically increase the complexity of our models from homogeneous material parameters up to the complex temperature-dependent coupling model presented in Sec. 5.3 to analyse the effect of each lithological entity on the rupture dynamics. As initial stresses, we keep the stresses that the SC model provides. This means that the stress difference between accretionary sediments and basalt is included in the initial stresses of all these models, even though the accretionary sediments themselves might not be included as an explicit material contrast. Here, we focus on the added effect of reflected and refracted waves from the free surface and material contrasts impacting the fault and reactivating fault slip. Compared to these effects, the stress inconsistency in the models with homogeneous material properties is of secondary importance as they are not observed to significantly alter the slip rate evolution. Hence, it does not affect any of our findings presented here. Fig. 11 shows the slip rate evolution for six models with an increasingly complex lithological structure as depicted by the insets. The corresponding final slip distribution is also indicated in each panel.

In the simplest model, we consider a homogeneous medium with basaltic material properties. We remove the free surface by extending the top boundary and placing absorbing boundary conditions on it (Fig. 11a). This effectively removes any reflections of the seismic waves from impedance contrasts or the free surface. The ensuing rupture is a supershear crack followed by a subshear crack. The crack-like nature of the rupture leads to a maximum slip accumulation in the nucleation region, which tapers towards the surface and brittle-ductile transition. The maximum slip that is reached in this homogeneous model is 29.5 m, which is twice as low as the maximum slip in the fully complex model of Sec. 5.3. The slip distribution is similar to the one from the SC model (Fig. 8c), which does not account for seismic waves. In the shallowest 100 km of the fault, the maximum slip is 16.7 m. This is more than 3 times less than in the model from Sec. 5.3, where the peak slip of 57.9 m is reached in the shallowest 100 km of the fault.

When a free surface is added to the model in Fig. 11a, the seismic waves reflect off of it. When they reach the fault, these reflections lower the normal stress on the fault. This results in an increase in fault slip rate and associated reactivation of fault slip (Fig. 11b). Because of the prolonged slip reactivation, the rupture duration and the total amount of slip on the fault increases. The slip is particularly increased in the shallow part of the fault where the reactivation of fault slip due to reflected waves is most pronounced.

When the incoming sediments of the accretionary wedge are added to the model in Fig. 11c, they introduce a low-velocity region, as the seismic velocities of the sediments are lower than that of the surrounding basalt. The impedance contrast between the sediments ($Z = 8.7 \cdot 10^6$ kg / s m^2) and basalt ($Z = 18.5 \cdot 10^6$ kg / s m^2) is large. This addition to the model results in a change of the rupture behaviour from predominantly crack-like to pulse-like. Pulse-like behaviour of the rupture is promoted by reflections that induce a stress change favourable for fault slip. Whether a reflection induces a positive or negative stress change depends on their polarity. When a stress change occurs that is unfavourable for slip, the slip on the fault stops which results in pulse-like behaviour (Huang et al., 2014).

The large impedance contrast also causes a large portion of the seismic waves to get trapped in the incoming sediments (also see Fig. 9). This results in a complex slip reactivation pattern on the fault that increases the accumulated slip on the fault in the sediments. The isolated patches of subducted sediment in the basalt in the vicinity of the sediment-basalt transition also cause a lot of wave reflections, refractions and interactions. This leads to pronounced rupture fronts in the basalt. Small nucleations in the sediments are facilitated by the low strength excess in the sediments.

The addition of lithospheric mantle changes the shape of the slip distribution (Fig. 11d). Waves reflecting from the free surface impact the deeper part of the fault less heavily than before, because the impedance contrast between the basaltic top layer and the lithospheric mantle is smaller and leads to less reflections. The lower wave amplitudes result in less fault slip reactivation in the basalt than in Fig. 11c. Therefore, the accumulated slip in the basaltic part of the fault is lower. The addition of lithospheric mantle also effectively transforms the deeper part of the fault that is going through the basalt into a low velocity region. However, the impedance contrast between the lithospheric mantle and the basalt is more than twice as low as the impedance contrast between the basalt and sediments. The effect of this lower velocity region is therefore not as pronounced as in Fig. 11c and we do not see pulse-like rupture behaviour in the basalt. The pulse-like behaviour of the rupture in the sediments is enhanced, even though the lithospheric mantle and the incoming sediments are not directly adjacent.

Adding asthenospheric mantle material to the model does not change any of the on-fault properties or the rupture. This is due to the low impedance contrast between lithospheric and asthenospheric mantle. Combined with the large distance between this impedance contrast and the fault, the on-fault effect of this material contrast is negligible on the rupture dynamics.

The addition of the accretionary wedge sediments adds a larger impedance contrast at the base of the wedge with the basalt (Fig. 11e). There is also an impedance contrast between the accretionary and incoming sediments, which causes additional reflections. This results in more reactivation of slip within the sediments.

The continental crust of the overriding plate is the last component of the SC subduction zone setup that we add to the model (Fig. 11f). Its addition results in less slip reactivation on the fault. Hence, the accumulated slip in Fig. 11f (maximum slip disregarding the unphysical slip peaks at isolated fault points is 59.2 m) is less than in Fig. 11e (maximum slip disregarding the unphysical slip peaks at isolated fault points is 61.4 m).

The models in Fig. 11 all assume constant material properties per rock type. However, one of the advantages of the SC model is that it provides temperature- and pressure-dependent densities. Comparing the model of Fig. 11f to Fig. 8d shows that the slip pulses on the fault are less pronounced when a temperature-dependent density is considered. This is due to less energetic reflections from decreased impedance contrasts related to the gradual increase of density and their related seismic velocities. Hence, the use of temperature-dependent properties leads to $\sim$ 1–2 m less slip on the fault.

In summary, these results show that material contrasts influence the rupture dynamics by causing slip reactivation on the fault and influencing the final slip distribution. The model with purely homogeneous material properties significantly underestimates the shallow fault slip by a factor 3 and results in a vastly different slip distribution. Using the temperature-dependent material contrasts of the SC model consistent with the fault geometry, stress, and yield stress, is crucial to resolve the complex wave interactions during rupture in a subduction zone which in turn affects the dynamics of the megathrust earthquake.

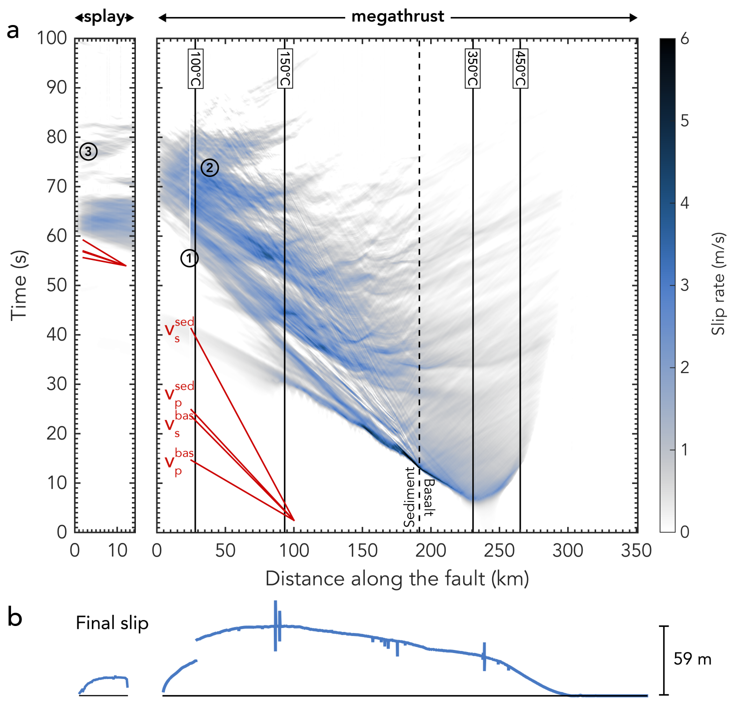

Figure 12. Slip rate evolution with time (a) and final accumulated slip (b) along the fault for both the splay fault (left column, note the horizontal exaggeration with respect to the megathrust fault x-axis) and the megathrust (right column). The splay fault connects to the megathrust at $x = 24.5$ km along the megathrust fault. Solid lines indicate the isotherms that define the frictional regimes; dashed line indicates material change. The P- and S-wave velocities v_p and v_s for both the basalt ($^{\text{bas}}$) and sediment ($^{\text{sed}}$) are indicated in red in both the splay and megathrust panels. Numbers are discussed in the text. The branching point on the megathrust and the two adjacent points to the left of the branching point are not plotted, as they show an unphysical numerical instability. Peak slip is indicated.

5.6 The impact of physically consistent stresses on splay fault activation

For simplicity, we only considered a rupture along the megathrust in the previous sections. However, the SC model shows high strain rate localisation along a splay fault instead of the shallow megathrust. However, the slip rates are not high enough to reach the threshold that defines a seismic event (Secs. 4.1 and 4.4). Here, we introduce the splay fault to the model by activating its internal frictional boundary condition so that slip on the splay fault is theoretically possible. This allows us to analyse if the splay fault is activated in the DR model when seismic waves are taken into account.

The resulting rupture evolution in terms of its slip rate and the final slip distribution of both the megathrust and splay fault are shown in Fig. 12. The splay fault in the DR model is activated at 56 s (Fig. 12a). Comparison with the reference model in Fig. 8 shows that both ruptures have a similar evolution. When the splay fault is activated at (1), the rupture chooses the splay fault over the megathrust and it continues at much lower slip rates on the megathrust than in the reference model ($\sim$ 56–68 s). This is also clearly illustrated in the final slip profile (Fig. 12b), as the final slip on the shallow megathrust is sharply reduced at the location of the splay fault compared to the reference model (Fig. 8f). Instead, we see 20 m of slip on the splay fault. When the splay fault is abandoned at approximately 68 s, the rupture in the shallow part of the megathrust looks very similar to the reference model results with the exception that small reflections from the splay fault on the megathrust are visible in the splay model (2). The last surface reflection at $\sim$ 74 s reactivates the splay fault (3). Combining the slip on the splay fault with that of the shallowest megathrust fault, we see that the same amount of slip is accumulated in total as on the megathrust in the DR model of Sec. 5.3.

In summary, our model shows that the splay fault is indeed activated in the DR model, depicting maximum slip rates of 2.4 m/s and a maximum slip of 20 m, which is much higher than what is observed in the corresponding SC model. Therefore, we need to account for additional fault complexities such as faults splaying off from the megathrust interface to fully assess the seismic and tsunami hazard of subduction zone earthquakes.

6 Discussion

By coupling a geodynamic seismic cycle model to a dynamic rupture model, we successfully modelled the geodynamic evolution of a subduction zone down to a single dynamic earthquake rupture of the megathrust. Broad rupture characteristics, such as the rupture nucleation, propagation, and arrest, of the SC event and its corresponding DR counterpart are qualitatively comparable. The seismic waves and a complicated subsurface structure affect the slip distribution on the fault, and the rupture style and duration. A homogeneous model significantly underestimates shallow fault slip, which has implications for tsunami hazard assessment. With our coupling method, we can also take into account complex fault geometries including splay faults. The complex resulting dynamic rupture highlights the need for taking all scales into account when assessing the seismic and tsunamigenic hazard of megathrust earthquakes.

In the following, we discuss our two most important coupling assumptions necessary to reconcile the SC and DR method. Namely, our choice of the Poisson's ratio, and the approximation of the SC model's rate-dependent friction by linear-slip weakening in the DR model. Lastly, we discuss limitations and future developments.

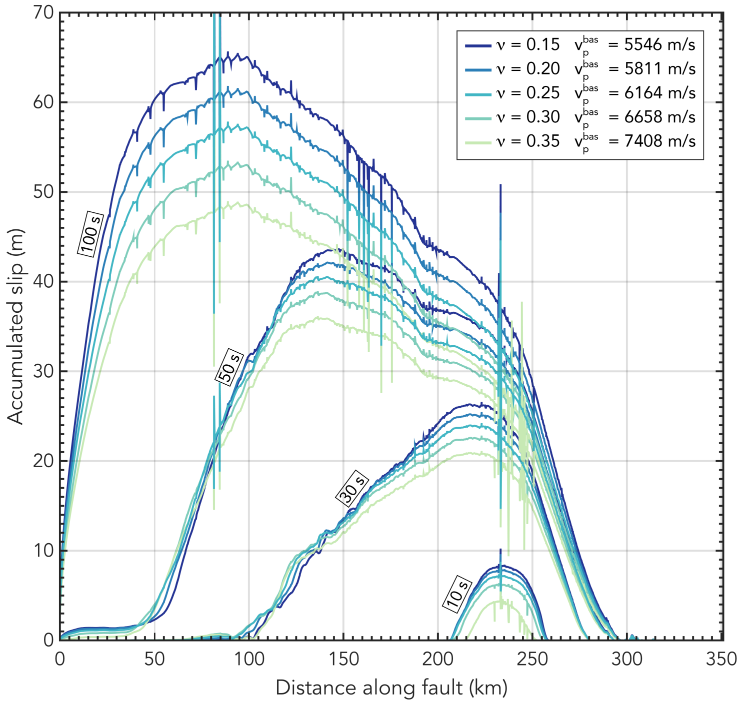

Figure 13. Accumulated slip along the fault plotted after 10 s, 30 s, 50 s and 100 s for five models where the first Lamé parameter was calculated using different Poisson's ratios. The corresponding change in P-wave velocity is indicated for the basalt. Note that the model with $\nu = 0.25$ is the model described in Sec. 5.3.

6.1 Effect of coupling choices

6.1.1 Poisson's ratio

To calculate the first Lamé parameter in the DR model from the incompressible SC model rock properties, we need to assume a Poisson's ratio. Computational seismology often uses Poisson solids as a simplification, where $\nu = 0.25$ and therefore $\lambda_1 = G$ (e.g., Stein & Wysession, 2009; Kozdon & Dunham, 2013). In line with this, we calculated λ_1 with $\nu = 0.25$ for our coupled event in Sec. 5. However, laboratory experiments indicate that there is a large variation in the Poisson's ratio of intact rocks, e.g., the Poisson's ratio of basalt ranges from 0.1–0.35 (Gercek, 2007).

An increase in Poisson's ratio results in an increase of the P-wave velocity v_p, and therefore increases the difference between the P- and S-wave velocities according to

$$v_p = v_s \sqrt{\frac{2\nu}{1 - 2\nu} + 2}. \tag{23}$$

To assess this effect on our results, we run several models with different Poisson's ratios. Models with Poisson's ratio $\nu > 0.40$ did not result in sustained nucleation and propagation of the rupture, due to the unrealistically large seismic velocities. For $\nu = 0.40$ several patches in the nucleation region are also already prohibited from rupturing. Fig. 13 shows the accumulated slip contours for several time steps for models with Poisson's ratio $0.15 - 0.35$. Larger Poisson's ratios result in less final slip with a maximum slip of 65.7 m for $\nu = 0.15$ and 49.0 m for $\nu = 0.35$, disregarding the unphysically high peaks in slip. This is due to a reduction in maximum slip rate and rupture duration. The latter is caused by both an increase in rupture speed and in nucleation time. The stress drop is not majorly affected by the Poisson's ratio.

Interestingly, as the slip decreases with increasing Poisson's ratio, the slip values of the DR model move towards those of the SC model, which has the highest possible Poisson's ratio of 0.5. Using a high Poisson's ratio for the model of Fig. 11a, where seismic wave effects are non-existent, would likely result in slip values similar to those of the SC model. This means that part of the slip difference between the SC and DR model can be accounted for by the difference in Poisson's ratio, while a factor of two to three of slip difference can be accounted for by fault reactivation due to wave reflections (Sec. 5.5).

The parameters affected by the Poisson's ratio (i.e., the maximum slip, rupture duration, slip rate, nucleation time, and rupture velocity) do not change the first order rupture characteristics, i.e., material dependent stress drop and predominantly updip rupture propagation, which are comparable to its SC rupture equivalent, or the rupture style.

6.1.2 Rate-dependent friction law approximation

In this study, we approximate the rate-dependent friction law of the SC model by a linear slip weakening friction law in the DR model. It is one of the simplest friction laws and it is widely used in the dynamic rupture community (e.g., Ma, 2012; Murphy et al., 2016). However, several other friction laws could have been used. For example, Olsen-Kettle et al. (2008) discusses the cubic, quintic, and septic slip weakening friction laws that are found to reduce the amount of slip.

Translating the rate-dependent friction formulation of the SC model to the linear slip weakening formulation of the DR model requires determining D_c. By ensuring that both friction laws have the same strength drop with slip (Secs. 4.5 and Fig. 5), we have a physical basis for picking a certain D_c value. The resultant D_c varies between 0.7–1.1 m in the sediments, which is in line with values used in the dynamic rupture community for similar problems (e.g., Goto et al., 2012; Murphy et al., 2016). The values for D_c in the basalt are slightly higher and range from 1.0–3.5 m with values from 0.7–3.0 m in the nucleation region.

An alternative way to couple the two friction laws would be to use the characteristic slip distance corresponding to the accumulated slip at which the lowest friction value is reached in the SC model (i.e., D_c would be larger in Fig. 5). To test the effect of D_c on our model results, we run models with a constant D_c along the fault varying from 0.25–8 m. We find that the nucleation phase takes longer for increasing D_c. This is consistent with work by Bizzarri et al. (2001). With constant $D_c \geq 4$ m, we do not get nucleation at all. Besides this effect on the nucleation phase of the model, increasing D_c results in a longer rupture duration accompanied by a smaller maximum slip velocity. Stress drop, maximum slip, and rupture speed are not significantly affected. As the choice of D_c does not affect the first-order rupture characteristics, we argue that using the D_c values obtained from equating the strength drop with slip between the two models results in robust rupture dynamics.

6.2 Limitations & future work

We observe large slip in the DR model, which is inconsistent with the recurrence time reported in Sec. 4.1 for the SC model. This is due to the fact that the recurrence interval is in line with the slip in the SC model which is lower than that of the DR model. The reasons for the differences in slip between the SC and DR model are (i)

the effect of seismic waves, as discussed in Sec. 5.5 and (*ii*) the difference in Poisson's ratio as discussed in Sec. 6.1.1. A future endeavour may be two-way coupling, i.e. transferring the final stress and strain conditions from the DR model back into the SC model, and analysing the effects on recurrence time.

At present, we couple the frictional parameters of the SC model to the discrete fault in the DR model. However, the SC model provides information on the stress field and material strength in the entire domain. This information can be used to extend the current DR model to account for plastic processes around the fault. Plasticity is found to influence the overall rupture dynamics, as well as the seafloor displacements (Ma, 2012), which will crucially affect the tsunamigenic potential of the faults. The DR model provides the ability to account for off-fault plastic deformation during coseismic rupture (Wollherr et al., 2018) and ongoing research is concentrated on coupling the off-fault plastic yielding of the SC model to that of the DR model (Wollherr, van Zelst, et al., 2019).

Another way to incorporate the large scale yielding in the accretionary wedge of the SC model relies on explicitly meshing the spontaneous splay faults of the SC model in the DR model. Besides coupling the on- and off-fault deformation between the SC and DR model in this manner, explicitly meshing the splay faults gives additional insight into the activation of splays in subduction zones and over several seismic cycles. Realistically modelling splay fault activation using the constraints from the SC model can also contribute to our understanding of tsunami generation.

Currently, the here presented coupling approach is restricted to two dimensions since the SC model is inherently two-dimensional. The extension of this coupling approach to three dimensions is on-going work within the ASCETE (Advanced Simulation of Coupled Earthquake and Tsunami Events) framework (E. Madden et al., 2019), where the two-dimensional initial conditions from the SC model are used in the three-dimensional version of SeisSol.

By extending our approach to three dimensions (e.g., Dunham & Bhat, 2008), accounting for off-fault plasticity (e.g., Gabriel et al., 2013), and reducing the friction drop between static and dynamic friction, we expect that the SC initial conditions are less favourable for supershear rupture. Changing the static friction to reduce the supershear rupture might also be a possibility, but we refrain from doing that in this work, because using a different friction coefficient while keeping the same stresses would lead to an inconsistency in the coupling of the yield criterion. This would negatively impact our achieved coupling in terms of stress drop. The high slip rate values observed in the DR models, which are typical for purely elastic dynamic rupture models (Andrews, 2005), may be limited by including off-fault plastic deformation.

Both the SC and DR model have advantages when it comes to hazard assessment. The SC model can provide insight into the recurrence interval and timing of earthquakes, whereas the DR model can provide accurate ground motions. With our coupled approach we combine these advantages and open new research avenues for further methodological advances that could ultimately lead to a three-dimensional coupled framework that includes physically consistent stress and slip for hazard assessment.

7 Conclusions

We couple geodynamic, seismic cycle, and dynamic rupture modelling to resolve a wide range of time scales governing megathrust earthquake ruptures. We use a two-dimensional, visco-elasto-plastic, continuum, seismo-thermo-mechanical model to simulate 4 Myrs of subduction dynamics and the subsequent seismic cycle. The long-term SC model geometry features a megathrust dipping at 14° on average and a large accretionary wedge due to sediment accretion. We model 70 quasi-periodic slip events in the seismic cycle phase, which mostly nucleate near the spontaneous down-dip limit of the seismogenic zone. The long-term constrained on-fault state of stress varies with lithology and reaches a maximum of 37.8 MPa just above the brittle-ductile transition. For the coupling, we use a representative SC slip event with maximum slip at the nucleation region near the down-dip limit of the seismogenic zone. The ductile regime is characterised by low stresses due to viscous stress relaxation and is accompanied by distributed ductile creep.

We then couple the full complexity of spatially heterogeneous, self-consistent fault stress and strength, material properties, and megathrust geometry at the onset of the SC slip event to a dynamic rupture model. The use of an unstructured triangular mesh allows for a complex megathrust geometry that results from the SC model. The dynamic rupture model resolves spontaneous earthquake rupture jointly with seismic waves in a two-dimensional elastic model of the megathrust interface.

The SC and DR events both nucleate and arrest spontaneously at the same locations. The stress drop in both models compares well and is material dependent, with sediments exhibiting a stress drop of $\sim$ 3 MPa in contrast to values of up to 10 MPa in basaltic regions.

The dynamic rupture propagates primarily updip in a crack-like fashion within the basalt and in a more pulse-like manner within the sediments. Both sections exhibit sustained supershear rupture speeds due to a small relative strength throughout the megathrust.

We systematically demonstrate the pronounced effects of complex lithological structures on rupture complexity, slip accumulation and dynamic fault reactivation. Removing all impedance contrasts that reflect waves decreases peak slip by a factor two. The homogeneous model shows a similar slip distribution to the SC model, which also does not account for reflecting seismic waves. The inclusion of an effective low-velocity zone in the form of sediments changes the rupture style from predominantly crack-like to pulse-like. In addition, seismic waves get trapped in the sediment layer which results in continuous reactivation of fault slip, particularly in the shallow part of the fault.

Within the presented coupling framework, we are able to include additional fault structures based on strain localisation in the SC model. Adding a splay fault to the dynamic rupture simulation results in preferred splay activation. Reflected waves also activate the megathrust.

Subduction zone geometry, lithology, fault stresses and strength, as constrained by subduction evolution and seismic cycles, crucially affect the first-order features of earthquake rupture dynamics. Our study also reveals important dynamic effects not captured in seismic cycle approaches, such as the effect of seismic wave reflections from the free surface on shallow slip accumulation in subduction zones. The SC results in terms of stress magnitude and variability constrained by 4 Myrs of subduction can be used as a guideline for setting up dynamic rupture models of subduction zone megathrusts and splay faults. This study highlights the key relationships between subduction zone processes and earthquake dynamics across temporal and spatial scales.

Appendix A Initial conditions governing the SC model

To initiate and sustain subduction, we apply a constant velocity of 7.5 cm/year to the subducting slab (Fig. 1), which is in line with observations for Southern Chile (Lallemand et al., 2005). Subduction initiation is further accommodated by a weak zone (Fig. 1), which follows a wet olivine flow law and has very low plastic strength (Table 2; Gerya & Meilick, 2011). After 3.2 million years, the initial weak zone is artificially removed and replaced with lithospheric mantle, so that the weaker material does not influence the model any more when a suitable subduction geometry has been obtained.

The initial temperature field is calculated by considering (*i*) the age of the subducting slab (40 Ma, Lallemand et al., 2005) according to the half space cooling model (Turcotte & Schubert, 2002), (*ii*) a linear temperature increase for the first 100 km of the continental crust from 0°C to 1300°C, and (*iii*) a 0.5°C km^{-1} temperature gradient in the asthenospheric mantle.

Appendix B Boundary conditions of the SC model

We adopt the same boundary conditions as van Dinther, Gerya, Dalguer, Mai, et al. (2013) with free slip boundary conditions at the sides, which allow material to freely move tangential to the boundaries, and an open boundary condition at the bottom (Fig. 1). To enhance the decoupling of the lithosphere from the boundaries, we use prescribed low viscosity regions at the side and bottom boundaries of the model (van Dinther, Gerya, Dalguer, Mai, et al., 2013). We apply viscosity limits of minimum $1 \cdot 10^{17}$ Pa s and maximum $1 \cdot 10^{25}$ Pa s throughout the model.

Due to the nature of the finite difference method, we do not have a true free surface in the SC model. Therefore, we use the sticky air method (Crameri et al., 2012), which is a widely used proxy for a free surface in finite difference geodynamics. The sticky air method consists of a layer of so-called 'sticky air' with low viscosity and density at the top of the model where the top boundary condition is free slip (Table 2). It allows the air-crust interface to behave as a free surface which can accommodate topography evolution.

The temperature is set to 0°C at the top of the domain and we impose zero heat flux at the sides. At the bottom boundary, we have a constant temperature boundary condition.

Appendix C Dominant deformation mechanism SC model at coupling time step

We evaluate the dominant deformation mechanism in the SC model at the coupling time step by looking at the visco-elasticity factor F, which is defined as

$$F = \frac{G\Delta t}{G\Delta t + \eta_{vp}} \tag{C1}$$

where G is the shear modulus, Δt is the time step, and η_{vp} is the effective visco-plastic viscosity. When there is no plastic deformation η_{vp} equals η (Eq. 8). Otherwise, when there is plastic deformation, η_{vp} equals $\eta \cdot \frac{\sigma'_{II}}{\eta\chi+\sigma'_{II}}$, where σ'_{II} is the second invariant of the deviatoric stress tensor and χ is the plastic multiplier. For purely elastic behaviour, F approaches 0, while F approaches 1 for purely viscous behaviour.

Fig. C1 shows the visco-elasticity factor of the SC model at the coupling time step (Sec. 4.1). It shows that stresses in the seismogenic zone (i.e., between 150°C and 350°C) are essentially completely elastic (i.e., $F < 0.05$). At higher temperatures the viscous component starts to increase slowly, which results from dislocation creep in the ductile regime. In the sticky air layer at the top of the model, the deformation mechanism is completely viscous such that the free surface does not interfere with the lithosphere (Crameri et al., 2012).

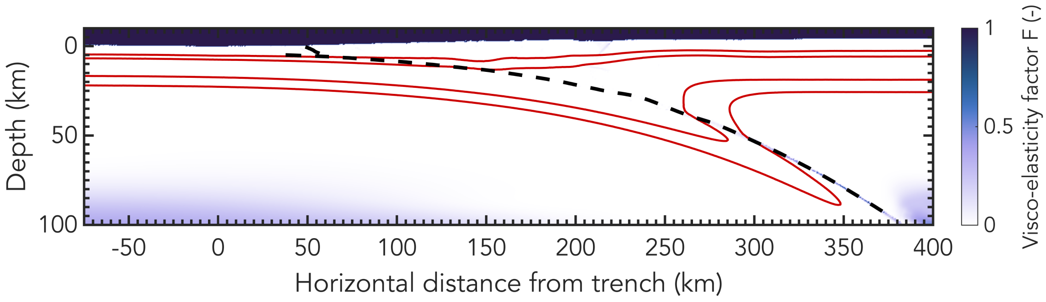

Figure C1. Visco-elasticity factor F in the SC model for the coupling time step. Faults are indicated by the dashed lines. The temperature contours, which define the frictional regimes and hence seismogenic zone, are indicated in red.

Appendix D Relative strength in the DR model

To estimate the initial closeness to failure of the fault, we can use several different measurements. In the geodynamics community, the strength excess is commonly used, which is the difference between the yield stress of the rock and the initial stresses (Fig. 7). In the dynamic rupture community it is more common to calculate the relative strength or so-called S parameter. We calculate the relative strength S for the DR model according to the following formula (Das & Aki, 1977a)

$$S = \frac{\tau_s - \tau_0}{\tau_0 - \tau_d} \tag{D1}$$

where $\tau_s = \sigma^{\mathrm{dr}}_{\mathrm{yield}} = c + \mu_s \sigma_n$ is the fault yield stress or initial static strength of the material (Sec. 3.2). $\tau_d = \sigma^{\mathrm{dr}}_{\mathrm{sliding}} = \sigma_n \mu_d$ is the sliding strength of the material, which can also be called the dynamic strength of the material. τ_0 is the initial shear stress. Note that the cohesion c does not enter the sliding strength of the fault. This is different to the SC model, where the bulk cohesion is always present in the yield criterion and strength of the material.

Fig. D1 shows that large parts of the fault are initially at failure with $S = 0$. However, these regions do not all result in sustained rupture, as discussed in Sec. 5.3. After ~ 15 s, the shallow part of the fault is no longer at failure, i.e. $S > 0$, although the relative strength is still very low, on the order of 0.05. When the main rupture arrives in the shallow part of the fault, it breaks again and S decreases to 0. The relative strength in the ductile regime is large ($S \gg 1$, up to 396), which prohibits rupture on that part of the fault.

A low relative strength promotes supershear pulses and cracks (e.g., Gabriel et al., 2012), which is indeed what occurs for the sustained main rupture in the DR model (Sec. 5.3). We note that the difference between initial loading stress and effective peak strength of the geodynamically constrained fault is on average well comparable to previous dynamic rupture models (e.g., Kozdon & Dunham, 2013). However, the large strength drop to low levels of dynamic sliding resistance causes the relative overall weakness in the DR model. The large strength drop in the DR model results from the 70% drop in friction used in the SC model (instead of e.g., 10% in Kozdon and Dunham (2013)) that features enhanced dynamic weakening as observed in laboratory experiments at seismic slip rates (e.g., Di Toro et al., 2011).

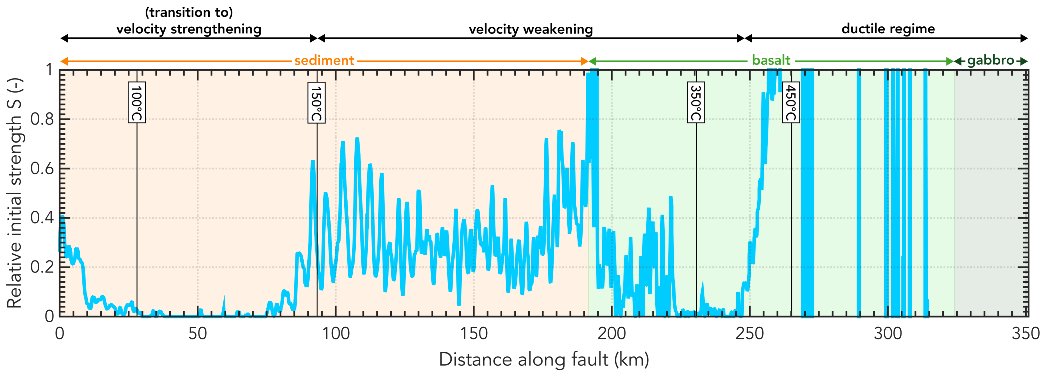

Figure D1. Relative strength S in the DR model along the fault. Frictional regimes dependent on temperature are indicated with corresponding isotherms (solid black lines). Background colours represent the material through which the fault is going.

Acknowledgments

We would like to thank Casper Pranger, Marie Bocher, Luca Dal Zilio, Simon Preuss, Claudio Petrini, and Robert Herrendörfer for fruitful discussions, insights into the SC models, and valuable comments that improved the manuscript. We would also like to thank Carsten Uphoff for providing a script to convert the DR mesh into the format required by SeisSol.

We also thank Brad Aagaard, an anonymous reviewer, associate editor Yoshihiro Kaneko, and editor Yehuda Ben-Zion for helpful comments that improved the manuscript.

Perceptually-uniform colour maps provided by Fabio Crameri and the cmocean package by Kristen Thyng were used in this study to prevent visual distortion of the data.

Computational resources were used on the CSCS clusters Mönch and Piz Daint (project no s741), and the ETH cluster Euler. Further computing resources were provided by the Institute of Geophysics of LMU Munich (Oeser et al., 2006) and the Leibniz Supercomputing Centre (LRZ, projects no h019z, pr63qo, and pr45fi on SuperMUC).

This work is part of the ASCETE project funded by the Volkswagen Foundation (Advanced Simulation of Coupled Earthquake-Tsunami Events, grant no 88479). YvD was funded by SNSF grants nos 200021153524 and 200021169880. SW and AAG were funded by the European Unions Horizon 2020 research and innovation program (ExaHyPE, grant no 671698 and ChEESE, grant no 823844), the German Research Foundation (DFG) (projects no KA 2281/4-1, GA 2465/2-1, GA 2465/3-1), BaCaTec (project no A4), and KONWIHR - the Bavarian Competence Network for Technical and Scientific High Performance Computing (project: NewWave).

IvZ developed the coupling method, designed the models, analysed the results, and wrote the article. YvD and AAG initiated and contributed to the concept development, suggested model setups, and supervised IvZ. SW and EHM contributed to the development of the coupling method. SW also provided additional features to the DR code specifically for the coupling method. All authors discussed the results and contributed to the final manuscript.

Input parameters for the SC model are discussed in Sec. 2.4, Appendix A and Appendix B, and Table 2. The DR model setup is discussed in 3.3. The complete input parameter file, megathrust and splay fault geometry, and surface geometry can be found in the Supporting Information.

References

Aagaard, B. T., Anderson, G., & Hudnut, K. W. (2004). Dynamic rupture modeling of the transition from thrust to strike-slip motion in the 2002 Denali fault earthquake, Alaska. *Bulletin of the Seismological Society of America*, *94*(6B), S190–S201.

Ampuero, J.-P., Vilotte, J.-P., & Sanchez-Sesma, F. (2002). Nucleation of rupture under slip dependent friction law: simple models of fault zone. *Journal of Geophysical Research: Solid Earth*, *107*(B12).

Andrews, D. (1973). A numerical study of tectonic stress release by underground explosions. *Bulletin of the Seismological Society of America*, *63*(4), 1375–1391.

Andrews, D. (2005). Rupture dynamics with energy loss outside the slip zone. *Journal of Geophysical Research: Solid Earth*, *110*(B1).

Angiboust, S., Wolf, S., Burov, E., Agard, P., & Yamato, P. (2012). Effect of fluid circulation on subduction interface tectonic processes: Insights from thermo-mechanical numerical modelling. *Earth and Planetary Science Letters*, *357*, 238–248.

Aochi, H., & Fukuyama, E. (2002). Three-dimensional nonplanar simulation of the 1992 Landers earthquake. *Journal of Geophysical Research: Solid Earth*, *107*(B2), ESE–4.

Bai, K., & Ampuero, J.-P. (2017). Effect of seismogenic depth and background stress on physical limits of earthquake rupture across fault step overs. *Journal of Geophysical Research: Solid Earth*, *122*(12).

Bauer, A., Scheipl, F., Küchenhoff, H., & Gabriel, A.-A. (2017). Modeling spatio-temporal earthquake dynamics using generalized functional additive regression. In *Proceedings of the 32nd international workshop on statistical modelling* (Vol. 2, pp. 146–149).

Belardinelli, M., Bizzarri, A., & Cocco, M. (2003). Earthquake triggering by static and dynamic stress changes. *Journal of Geophysical Research: Solid Earth*, *108*(B3).

Ben-Zion, Y., & Rice, J. R. (1997). Dynamic simulations of slip on a smooth fault in an elastic solid. *Journal of Geophysical Research: Solid Earth*, *102*(B8), 17771–17784.

Billen, M. I. (2008). Modeling the dynamics of subducting slabs. *Annual Review of Earth and Planetary Sciences*, *36*, 325–356.

Billen, M. I., Gurnis, M., & Simons, M. (2003). Multiscale dynamics of the Tonga-Kermadec subduction zone. *Geophysical Journal International*, *153*(2), 359–388.

Bizzarri, A. (2010). How to promote earthquake ruptures: Different nucleation strategies in a dynamic model with slip-weakening friction. *Bulletin of the Seismological Society of America*, *100*(3), 923–940.

Bizzarri, A., Cocco, M., Andrews, D., & Boschi, E. (2001). Solving the dynamic rupture problem with different numerical approaches and constitutive laws. *Geophysical Journal International*, *144*(3), 656–678.

Blanpied, M. L., Lockner, D. A., & Byerlee, J. D. (1995). Frictional slip of granite at hydrothermal conditions. *Journal of Geophysical Research: Solid Earth*, *100*(B7), 13045–13064.

Bormann, P., Engdahl, B., & Kind, R. (2012). Seismic wave propagation and earth models. In P. Bormann (Ed.), *New Manual of Seismological Observatory Prac-*

tice 2 (NMSOP2) (p. 1 - 105). Potsdam : Deutsches GeoForschungsZentrum GFZ.

Brune, J. N. (1970). Tectonic stress and the spectra of seismic shear waves from earthquakes. *Journal of geophysical research*, *75* (26), 4997–5009.

Buiter, S. J., Schreurs, G., Albertz, M., Gerya, T. V., Kaus, B., Landry, W., … others (2016). Benchmarking numerical models of brittle thrust wedges. *Journal of structural geology*, *92*, 140–177.

Chang, C., McNeill, L. C., Moore, J. C., Lin, W., Conin, M., & Yamada, Y. (2010). In situ stress state in the Nankai accretionary wedge estimated from borehole wall failures. *Geochemistry, Geophysics, Geosystems*, *11* (12).

Chester, F., & Higgs, N. (1992). Multimechanism friction constitutive model for ultrafine quartz gouge at hypocentral conditions. *Journal of Geophysical Research: Solid Earth*, *97* (B2), 1859–1870.

Cisternas, M., Atwater, B. F., Torrejón, F., Sawai, Y., Machuca, G., Lagos, M., … others (2005). Predecessors of the giant 1960 Chile earthquake. *Nature*, *437* (7057), 404.

Corbi, F., Funiciello, F., Brizzi, S., Lallemand, S., & Rosenau, M. (2017). Control of asperities size and spacing on seismic behavior of subduction megathrusts. *Geophysical Research Letters*, *44*.

Crameri, F., Schmeling, H., Golabek, G. J., Duretz, T., Orendt, R., Buiter, S. J. H., … Tackley, P. J. (2012). A comparison of numerical surface topography calculations in geodynamic modelling: an evaluation of the 'sticky air' method. *Geophysical Journal International*, *189* (1), 38–54.

Dalguer, L. A., & Day, S. M. (2007). Staggered-grid split-node method for spontaneous rupture simulation. *Journal of Geophysical Research: Solid Earth*, *112* (B2).

Dal Zilio, L., van Dinther, Y., Gerya, T. V., & Avouac, J.-P. (2019). Bimodal seismicity in the Himalaya controlled by fault friction and geometry. *Nature communications*, *10* (1), 48.

Dal Zilio, L., van Dinther, Y., Gerya, T. V., & Pranger, C. C. (2018). Seismic behaviour of mountain belts controlled by plate convergence rate. *Earth and Planetary Science Letters*, *482*, 81–92.

Das, S. (1980). A numerical method for determination of source time functions for general three-dimensional rupture propagation. *Geophysical Journal International*, *62* (3), 591–604.

Das, S., & Aki, K. (1977a). Fault plane with barriers: a versatile earthquake model. *Journal of geophysical research*, *82* (36), 5658–5670.

Das, S., & Aki, K. (1977b). A numerical study of two-dimensional spontaneous rupture propagation. *Geophysical Journal of the Royal Astronomical Society*, *50* (3), 643–668.

Day, S. M. (1982). Three-dimensional finite difference simulation of fault dynamics: rectangular faults with fixed rupture velocity. *Bulletin of the Seismological Society of America*, *72* (3), 705–727.

DeDontney, N., & Hubbard, J. (2012). Applying wedge theory to dynamic rupture modeling of fault junctions. *Bulletin of the Seismological Society of America*, *102* (4), 1693–1711.

DeDontney, N., & Rice, J. R. (2012). Tsunami wave analysis and possibility of splay fault rupture during the 2004 Indian Ocean earthquake. *Pure and applied geophysics*, *169* (10), 1707–1735.

DeDontney, N., Rice, J. R., & Dmowska, R. (2012). Finite element modeling of branched ruptures including off-fault plasticity. *Bulletin of the Seismological Society of America*, *102* (2), 541–562.

de la Puente, J., Ampuero, J.-P., & Käser, M. (2009). Dynamic rupture modeling on unstructured meshes using a discontinuous Galerkin method. *Journal of Geophysical Research: Solid Earth*, *114* (B10).

Del Gaudio, P., Di Toro, G., Han, R., Hirose, T., Nielsen, S., Shimamoto, T., & Cavallo, A. (2009). Frictional melting of peridotite and seismic slip. *Journal of Geophysical Research: Solid Earth*, *114*(B6).

den Hartog, S. A., Peach, C. J., de Winter, D. M., Spiers, C. J., & Shimamoto, T. (2012). Frictional properties of megathrust fault gouges at low sliding velocities: New data on effects of normal stress and temperature. *Journal of Structural Geology*, *38*, 156–171.

Den Hartog, S. A. M., Niemeijer, A. R., & Spiers, C. J. (2012). New constraints on megathrust slip stability under subduction zone P–T conditions. *Earth and Planetary Science Letters*, *353*, 240–252.

Dieterich, J. H. (1978). Time-dependent friction and the mechanics of stick-slip. In *Rock friction and earthquake prediction* (pp. 790–806). Springer.

Dieterich, J. H. (1979). Modeling of rock friction: 1. experimental results and constitutive equations. *Journal of Geophysical Research: Solid Earth*, *84*(B5), 2161–2168.

Di Toro, G., Han, R., Hirose, T., De Paola, N., Nielsen, S., Mizoguchi, K., ... Shimamoto, T. (2011). Fault lubrication during earthquakes. *Nature*, *471*(7339), 494.

Drucker, D. C., & Prager, W. (1952). Soil mechanics and plastic analysis or limit design. *Quarterly of applied mathematics*, *10*(2), 157–165.

Dumbser, M., & Käser, M. (2006). An arbitrary high-order discontinuous Galerkin method for elastic waves on unstructured meshes-II. The three-dimensional isotropic case. *Geophysical Journal International*, *167*(1), 319–336.

Dunham, E. M., & Bhat, H. S. (2008). Attenuation of radiated ground motion and stresses from three-dimensional supershear ruptures. *Journal of Geophysical Research: Solid Earth*, *113*(B8).

Fujiwara, T., Kodaira, S., No, T., Kaiho, Y., Takahashi, N., & Kaneda, Y. (2011). The 2011 Tohoku-Oki earthquake: Displacement reaching the trench axis. *Science*, *334*(6060), 1240–1240.

Fukao, Y. (1979). Tsunami earthquakes and subduction processes near deep-sea trenches. *Journal of Geophysical Research: Solid Earth*, *84*(B5), 2303–2314.

Fulton, P., Brodsky, E. E., Kano, Y., Mori, J., Chester, F., Ishikawa, T., ... others (2013). Low coseismic friction on the Tohoku-Oki fault determined from temperature measurements. *Science*, *342*(6163), 1214–1217.

Gabriel, A.-A., Ampuero, J.-P., Dalguer, L. A., & Mai, P. M. (2012). The transition of dynamic rupture styles in elastic media under velocity-weakening friction. *Journal of Geophysical Research: Solid Earth*, *117*(B9).

Gabriel, A.-A., Ampuero, J.-P., Dalguer, L. A., & Mai, P. M. (2013, aug). Source Properties of Dynamic Rupture Pulses with Off-Fault Plasticity. *Journal of Geophysical Research: Solid Earth*, *118*(8), 4117–4126.

Gabriel, A.-A., & Pelties, C. (2014). Simulating Large-Scale Earthquake Dynamic Rupture Scenarios On Natural Fault Zones Using the ADER-DG Method. In *Geophysical Research Abstracts, EGU General Assembly 2014* (Vol. 16, p. EGU2014-10572).

Galis, M., Pelties, C., Kristek, J., Moczo, P., Ampuero, J.-P., & Mai, P. M. (2014). On the initiation of sustained slip-weakening ruptures by localized stresses. *Geophysical Journal International*, *200*(2), 890–909.

Galvez, P., Ampuero, J.-P., Dalguer, L. A., Somala, S. N., & Nissen-Meyer, T. (2014). Dynamic earthquake rupture modelled with an unstructured 3-D spectral element method applied to the 2011 M 9 Tohoku earthquake. *Geophysical Journal International*, *198*(2), 1222–1240.

Galvez, P., Peter, D. B., & Mai, P. M. (2018). Earthquake cycle modeling of curvilinear non-planar faults: 1992, Landers earthquake sequence. In *AGU Fall Meeting Abstracts.*

Gercek, H. (2007). Poisson's ratio values for rocks. *International Journal of Rock*

Mechanics and Mining Sciences, *44*(1), 1–13.

Gerya, T. V. (2010). *Introduction to numerical geodynamic modelling.* Cambridge University Press.

Gerya, T. V. (2011). Future directions in subduction modeling. *Journal of Geodynamics*, *52*(5), 344–378.

Gerya, T. V., & Meilick, F. (2011). Geodynamic regimes of subduction under an active margin: effects of rheological weakening by fluids and melts. *Journal of Metamorphic Geology*, *29*(1), 7–31.

Gerya, T. V., & Yuen, D. A. (2003). Characteristics-based marker-in-cell method with conservative finite-differences schemes for modeling geological flows with strongly variable transport properties. *Physics of the Earth and Planetary Interiors*, *140*(4), 293–318.

Gerya, T. V., & Yuen, D. A. (2007). Robust characteristics method for modelling multiphase visco-elasto-plastic thermo-mechanical problems. *Physics of the Earth and Planetary Interiors*, *163*(1), 83–105.

Geuzaine, C., & Remacle, J.-F. (2009). Gmsh: A 3-D finite element mesh generator with built-in pre-and post-processing facilities. *International journal for numerical methods in engineering*, *79*(11), 1309–1331.

Goes, S., Agrusta, R., van Hunen, J., & Garel, F. (2017). Subduction-transition zone interaction: A review. *Geosphere*, *13*(3), 644–664.

Goto, H., Yamamoto, Y., & Kita, S. (2012). Dynamic rupture simulation of the 2011 off the Pacific coast of Tohoku Earthquake: Multi-event generation within dozens of seconds. *Earth, planets and space*, *64*(12), 11.

Hardebeck, J. L. (2012). Coseismic and postseismic stress rotations due to great subduction zone earthquakes. *Geophysical Research Letters*, *39*(21).

Hardebeck, J. L. (2015). Stress orientations in subduction zones and the strength of subduction megathrust faults. *Science*, *349*(6253), 1213–1216.

Harris, R. A. (2004). Numerical simulations of large earthquakes: Dynamic rupture propagation on heterogeneous faults. In A. Donnellan, P. Mora, M. Matsu'ura, & X.-C. Yin (Eds.), *Computational earthquake science part ii* (pp. 2171–2181). Basel: Birkhäuser Basel. doi: 10.1007/978-3-0348-7875-3_5

Harris, R. A., Barall, M., Aagaard, B., Ma, S., Roten, D., Olsen, K., … Dalguer, L. (2018). A suite of exercises for verifying dynamic earthquake rupture codes. *Seismological Research Letters*, *89*(3), 1146.

Harris, R. A., Barall, M., Andrews, D., Duan, B., Ma, S., Dunham, E., … others (2011). Verifying a computational method for predicting extreme ground motion. *Seismological Research Letters*, *82*(5), 638–644.

Harris, R. A., Barall, M., Archuleta, R., Dunham, E., Aagaard, B., Ampuero, J., … others (2009). The SCEC/USGS dynamic earthquake rupture code verification exercise. *Seismological Research Letters*, *80*(1), 119–126.

Heinecke, A., Breuer, A., Rettenberger, S., Bader, M., Gabriel, A.-A., Pelties, C., … others (2014). Petascale high order dynamic rupture earthquake simulations on heterogeneous supercomputers. In *SC14: Proceedings of the International Conference for High Performance Computing, Networking, Storage and Analysis* (pp. 3–14).

Herrendörfer, R. (2018). *Modeling of the slip spectrum along mature and spontaneously forming faults in a visco-elasto-plastic continuum* (Unpublished doctoral dissertation). ETH Zurich.

Herrendörfer, R., Gerya, T. V., & van Dinther, Y. (2018). An invariant rate-and state-dependent friction formulation for visco-elasto-plastic earthquake cycle simulations. *Journal of Geophysical Research: Solid Earth*.

Herrendörfer, R., Van Dinther, Y., Gerya, T. V., & Dalguer, L. A. (2015). Earthquake supercycle in subduction zones controlled by the width of the seismogenic zone. *Nature Geoscience*, *8*(6), 471.

Huang, Y., Ampuero, J.-P., & Helmberger, D. V. (2014). Earthquake ruptures

modulated by waves in damaged fault zones. *Journal of Geophysical Research: Solid Earth*, *119*(4), 3133–3154.
Huang, Y., Meng, L., & Ampuero, J.-P. (2013). A dynamic model of the frequency-dependent rupture process of the 2011 Tohoku-Oki earthquake. *Earth, planets and space*, *64*(12), 1.
Ida, Y. (1973). The maximum acceleration of seismic ground motion. *Bulletin of the Seismological Society of America*, *63*(3), 959–968.
Kame, N., Rice, J. R., & Dmowska, R. (2003). Effects of prestress state and rupture velocity on dynamic fault branching. *Journal of Geophysical Research: Solid Earth*, *108*(B5).
Kaneko, Y., Ampuero, J.-P., & Lapusta, N. (2011). Spectral-element simulations of long-term fault slip: Effect of low-rigidity layers on earthquake-cycle dynamics. *Journal of Geophysical Research: Solid Earth*, *116*(B10).
Kaus, B. J. (2010). Factors that control the angle of shear bands in geodynamic numerical models of brittle deformation. *Tectonophysics*, *484*(1-4), 36–47.
Kodaira, S., Kurashimo, E., Park, J.-O., Takahashi, N., Nakanishi, A., Miura, S., … Kaneda, Y. (2002). Structural factors controlling the rupture process of a megathrust earthquake at the Nankai trough seismogenic zone. *Geophysical Journal International*, *149*(3), 815–835.
Kopf, A., & Brown, K. M. (2003). Friction experiments on saturated sediments and their implications for the stress state of the Nankai and Barbados subduction thrusts. *Marine Geology*, *202*(3-4), 193–210.
Kostrov, B. V. (1964). Self similar problems of propagation of shear cracks. *Journal of Applied Mathematics and Mechanics*, *28*(5), 1077–1087.
Kozdon, J. E., & Dunham, E. M. (2013). Rupture to the trench: Dynamic rupture simulations of the 11 March 2011 Tohoku earthquake. *Bulletin of the Seismological Society of America*, *103*(2B), 1275–1289.
Kozdon, J. E., Dunham, E. M., & Nordström, J. (2013). Simulation of dynamic earthquake ruptures in complex geometries using high-order finite difference methods. *Journal of Scientific Computing*, *55*(1), 92–124.
Lallemand, S., Heuret, A., & Boutelier, D. (2005). On the relationships between slab dip, back-arc stress, upper plate absolute motion, and crustal nature in subduction zones. *Geochemistry, Geophysics, Geosystems*, *6*(9).
Langer, S., Olsen-Kettle, L. M., Weatherley, D., Gross, L., & Mühlhaus, H.-B. (2010). Numerical studies of quasi-static tectonic loading and dynamic rupture of bi-material interfaces. *Concurrency and Computation: Practice and Experience*, *22*(12), 1684–1702.
Lapusta, N., Rice, J. R., Ben-Zion, Y., & Zheng, G. (2000). Elastodynamic analysis for slow tectonic loading with spontaneous rupture episodes on faults with rate-and state-dependent friction. *Journal of Geophysical Research: Solid Earth*, *105*(B10), 23765–23789.
Lay, T., Ammon, C. J., Kanamori, H., Xue, L., & Kim, M. J. (2011). Possible large near-trench slip during the 2011 Mw 9.0 off the Pacific coast of Tohoku Earthquake. *Earth, planets and space*, *63*(7), 32.
Li, S., Moreno, M., Rosenau, M., Melnick, D., & Oncken, O. (2014). Splay fault triggering by great subduction earthquakes inferred from finite element models. *Geophysical Research Letters*, *41*(2), 385–391.
Liu, Y., & Rice, J. R. (2007). Spontaneous and triggered aseismic deformation transients in a subduction fault model. *Journal of Geophysical Research: Solid Earth*, *112*(B9).
Lotto, G. C., Dunham, E. M., Jeppson, T. N., & Tobin, H. J. (2017). The effect of compliant prisms on subduction zone earthquakes and tsunamis. *Earth and Planetary Science Letters*, *458*, 213–222.
Ma, S. (2012). A self-consistent mechanism for slow dynamic deformation and tsunami generation for earthquakes in the shallow subduction zone. *Geophysi-*

cal Research Letters, *39*(11).
Madariaga, R., Olsen, K., & Archuleta, R. (1998). Modeling dynamic rupture in a 3D earthquake fault model. *Bulletin of the Seismological Society of America*, *88*(5), 1182–1197.
Madden, E., Bader, M., Behrens, J., van Dinther, Y., Gabriel, A.-A., Rannabauer, L., … et al. (2019, Sep). *Methods and test cases for linking physics-based earthquake and tsunami models.* EarthArXiv. Retrieved from `eartharxiv.org/rzvn2` doi: 10.31223/osf.io/rzvn2
Madden, E. H., Ulrich, T., Gabriel, A.-A., van Zelst, I., & van Dinther, Y. (2017). The role of splay faults in seafloor deformation and tsunami generation during the Mw 9.1-9.3 Sumatra-Andaman Earthquake. In E. E. Gdoutos (Ed.), *Proceedings of the 14th international conference on fracture.*
Moresi, L., Dufour, F., & Mühlhaus, H.-B. (2003). A Lagrangian integration point finite element method for large deformation modeling of viscoelastic geomaterials. *Journal of computational physics*, *184*(2), 476–497.
Murphy, S., Scala, A., Herrero, A., Lorito, S., Festa, G., Trasatti, E., … Nielsen, S. (2016). Shallow slip amplification and enhanced tsunami hazard unravelled by dynamic simulations of mega-thrust earthquakes. *Scientific reports*, *6*, 35007.
Nielsen, S., & Madariaga, R. (2003). On the self-healing fracture mode. *Bulletin of the Seismological Society of America*, *93*(6), 2375–2388.
Oeser, J., Bunge, H.-P., & Mohr, M. (2006). Cluster design in the earth sciences: Tethys. In *International conference on high performance computing and communications* (pp. 31–40).
Oglesby, D. D., Archuleta, R. J., & Nielsen, S. B. (1998). Earthquakes on dipping faults: the effects of broken symmetry. *Science*, *280*(5366), 1055–1059.
Olsen-Kettle, L., Weatherley, D., Saez, E., Gross, L., Mühlhaus, H.-B., & Xing, H. (2008). Analysis of slip-weakening frictional laws with static restrengthening and their implications on the scaling, asymmetry, and mode of dynamic rupture on homogeneous and bimaterial interfaces. *Journal of Geophysical Research: Solid Earth*, *113*(B8).
Patočka, V., Čadek, O., Tackley, P. J., & Čížková, H. (2017). Stress memory effect in viscoelastic stagnant lid convection. *Geophysical Journal International*, *209*(3), 1462–1475.
Pelties, C., Gabriel, A.-A., & Ampuero, J.-P. (2014). Verification of an ADER-DG method for complex dynamic rupture problems. *Geoscientific Model Development*, *7*(3), 847–866.
Pelties, C., Huang, Y., & Ampuero, J.-P. (2015). Pulse-like rupture induced by three-dimensional fault zone flower structures. *Pure and Applied Geophysics*, *172*(5), 1229–1241.
Pelties, C., Puente, J., Ampuero, J.-P., Brietzke, G. B., & Käser, M. (2012). Three-dimensional dynamic rupture simulation with a high-order discontinuous Galerkin method on unstructured tetrahedral meshes. *Journal of Geophysical Research: Solid Earth*, *117*(B2).
Petrini, C., Gerya, T. V., van Dinther, Y., Connolly, J. A., & Madonna, C. (2017). Modelling earthquakes using a poro-elastic two-phase flow formulation. In *AGU Fall Meeting Abstracts.*
Pollard, D. D., & Fletcher, R. C. (2005). *Fundamentals of structural geology.* Cambridge University Press.
Preuss, S., Herrendörfer, R., Gerya, T., Ampuero, J.-P., & van Dinther, Y. (2019). Seismic and aseismic fault growth lead to different fault orientations. *Journal of Geophysical Research: Solid Earth*, *124*. Retrieved from `https://agupubs.onlinelibrary.wiley.com/doi/abs/10.1029/2019JB017324` doi: 10.1029/2019JB017324
Ranalli, G. (1995). *Rheology of the earth.* Springer Science & Business Media.
Rice, J. R. (1993). Spatio-temporal complexity of slip on a fault. *Journal of Geo-*

physical Research: Solid Earth, *98*(B6), 9885–9907.
Romanet, P., Bhat, H. S., Jolivet, R., & Madariaga, R. (2018). Fast and slow slip events emerge due to fault geometrical complexity. *Geophysical Research Letters*, *45*(10), 4809–4819.
Ruina, A. (1983). Slip instability and state variable friction laws. *Journal of Geophysical Research: Solid Earth*, *88*(B12), 10359–10370.
Schultz, R. (1995). Limits on strength and deformation properties of jointed basaltic rock masses. *Rock Mechanics and Rock Engineering*, *28*(1), 1–15.
Seno, T. (2009). Determination of the pore fluid pressure ratio at seismogenic megathrusts in subduction zones: Implications for strength of asperities and Andean-type mountain building. *Journal of Geophysical Research: Solid Earth*, *114*(B5).
Sobolev, S. V., & Muldashev, I. A. (2017). Modeling seismic cycles of great megathrust earthquakes across the scales with focus at postseismic phase. *Geochemistry, Geophysics, Geosystems*, *18*(12), 4387–4408.
Stein, S., & Wysession, M. (2009). *An introduction to seismology, earthquakes, and earth structure*. John Wiley & Sons.
Tamura, S., & Ide, S. (2011). Numerical study of splay faults in subduction zones: The effects of bimaterial interface and free surface. *Journal of Geophysical Research: Solid Earth*, *116*(B10).
Tsutsumi, A., & Shimamoto, T. (1997). High-velocity frictional properties of gabbro. *Geophysical Research Letters*, *24*(6), 699–702.
Turcotte, D., & Schubert, G. (2002). *Geodynamics*. Cambridge University Press.
Ujiie, K., Tanaka, H., Saito, T., Tsutsumi, A., Mori, J. J., Kameda, J., … Scientists, T. (2013). Low Coseismic Shear Stress on the Tohoku-Oki Megathrust Determined from Laboratory Experiments. *Science*, *342*(6163), 1211–1214. doi: 10.1126/science.1243485
Ulrich, T., Gabriel, A.-A., Ampuero, J.-P., & Xu, W. (2019). Dynamic viability of the 2016 mw 7.8 kaikōura earthquake cascade on weak crustal faults. *Nature communications*, *10*(1), 1213.
Ulrich, T., Vater, S., Madden, E. H., Behrens, J., van Dinther, Y., van Zelst, I., … Gabriel, A.-A. (2019). Coupled, physics-based modeling reveals earthquake displacements are critical to the 2018 palu, sulawesi tsunami. *Pure and Applied Geophysics*, 1–41.
Uphoff, C., Rettenberger, S., Bader, M., Madden, E. H., Ulrich, T., Wollherr, S., & Gabriel, A.-A. (2017). Extreme scale multi-physics simulations of the tsunamigenic 2004 sumatra megathrust earthquake. In *Proceedings of the international conference for high performance computing, networking, storage and analysis* (p. 21).
van Dinther, Y., Gerya, T. V., Dalguer, L. A., Corbi, F., Funiciello, F., & Mai, P. M. (2013). The seismic cycle at subduction thrusts: 2. Dynamic implications of geodynamic simulations validated with laboratory models. *Journal of Geophysical Research: Solid Earth*, *118*(4), 1502–1525.
van Dinther, Y., Gerya, T. V., Dalguer, L. A., Mai, P. M., Morra, G., & Giardini, D. (2013). The seismic cycle at subduction thrusts: Insights from seismo-thermo-mechanical models. *Journal of Geophysical Research: Solid Earth*, *118*(12), 6183–6202.
van Dinther, Y., Mai, P. M., Dalguer, L. A., & Gerya, T. V. (2014). Modeling the seismic cycle in subduction zones: The role and spatiotemporal occurrence of off-megathrust earthquakes. *Geophysical Research Letters*, *41*(4), 1194–1201.
Wang, K., & Hu, Y. (2006). Accretionary prisms in subduction earthquake cycles: The theory of dynamic Coulomb wedge. *Journal of Geophysical Research: Solid Earth*, *111*(B6).
Wendt, J., Oglesby, D. D., & Geist, E. L. (2009). Tsunamis and splay fault dynamics. *Geophysical Research Letters*, *36*(15).

Wollherr, S., Gabriel, A.-A., & Mai, P. M. (2019). Landers 1992 “reloaded”: Integrative dynamic earthquake rupture modeling. *Journal of Geophysical Research: Solid Earth*.

Wollherr, S., Gabriel, A.-A., & Uphoff, C. (2018). Off-fault plasticity in three-dimensional dynamic rupture simulations using a modal Discontinuous Galerkin method on unstructured meshes: Implementation, verification, and application. *Geophysical Journal International*, *214*, 1556–1584. doi: https://doi.org/10.1093/gji/ggy213

Wollherr, S., van Zelst, I., Gabriel, A.-A., Madden, E. H., & van Dinther, Y. (2019). Plastic deformation and seafloor uplift in geomechanically constrained dynamic rupture models of subduction zone earthquakes. In *EGU General Assembly Abstracts.*